REPORT DOCUMENTATION PAGE

Form Approved OMB NO. 0704-0188

The public reporting burden for this collection of information is estimated to average 1 hour per response, including the time for reviewing instructions, searching existing data sources, gathering and maintaining the data needed, and completing and reviewing the collection of information. Send comments regarding this burden estimate or any other aspect of this collection of information, including suggesstions for reducing this burden, to Washington Headquarters Services, Directorate for Information Operations and Reports, 1215 Jefferson Davis Highway, Suite 1204, Arlington VA, 22202-4302. Respondents should be aware that notwithstanding any other provision of law, no person shall be subject to any oenalty for failing to comply with a collection of information if it does not display a currently valid OMB control number.
PLEASE DO NOT RETURN YOUR FORM TO THE ABOVE ADDRESS.

1. REPORT DATE (DD-MM-YYYY)	2. REPORT TYPE	3. DATES COVERED (From - To)
09-10-2007	Final Report	14-Jun-2004 - 13-Jun-2007

4. TITLE AND SUBTITLE
Mode Locking of Quantum Cascade Lasers

5a. CONTRACT NUMBER
W911NF-04-1-0253

5b. GRANT NUMBER

5c. PROGRAM ELEMENT NUMBER
611102

6. AUTHORS
Federico Capasso, Franz Kaertner

5d. PROJECT NUMBER

5e. TASK NUMBER

5f. WORK UNIT NUMBER

7. PERFORMING ORGANIZATION NAMES AND ADDRESSES
Harvard College
Office of Sponsored Research
1350 Massachusetts Ave. Holyoke 727
Cambridge, MA 02138 -

8. PERFORMING ORGANIZATION REPORT NUMBER

9. SPONSORING/MONITORING AGENCY NAME(S) AND ADDRESS(ES)
U.S. Army Research Office
P.O. Box 12211
Research Triangle Park, NC 27709-2211

10. SPONSOR/MONITOR'S ACRONYM(S)
ARO

11. SPONSOR/MONITOR'S REPORT NUMBER(S)
46692-PH.7

12. DISTRIBUTION AVAILIBILITY STATEMENT
Approved for public release; Federal purpose rights

13. SUPPLEMENTARY NOTES
The views, opinions and/or findings contained in this report are those of the author(s) and should not contrued as an official Department of the Army position, policy or decision, unless so designated by other documentation.

14. ABSTRACT
A theoretical and experimental study of multimode operation regimes in quantum cascade lasers (QCLs) is presented. It is shown that the fast gain recovery of QCLs promotes two multimode regimes in QCLs: One is spatial hole burning (SHB), and the other one is related to the Risken-Nummedal-Graham-Haken (RNGH) instability predicted in the sixties. A model that can account for coherent phenomena, a saturable absorber and SHB is developed and studied in detail both analytically and numerically. A wide variety of experimental data on multimode regimes is presented. Lasers with narrow active region and/or with metal coating on the sides tend to develop a splitting in the spectrum, approximately equal to twice the Rabi frequency. It

15. SUBJECT TERMS
quantum cascade lasers, coherent instability, multimode operation, modelocking, high power, mid-infrared

16. SECURITY CLASSIFICATION OF:			17. LIMITATION OF ABSTRACT	15. NUMBER OF PAGES	19a. NAME OF RESPONSIBLE PERSON
a. REPORT	b. ABSTRACT	c. THIS PAGE			Federico Capasso
U	U	U	SAR		19b. TELEPHONE NUMBER 617-384-7611

Report Title

Mode Locking of Quantum Cascade Lasers

ABSTRACT

A theoretical and experimental study of multimode operation regimes in quantum cascade lasers (QCLs) is presented. It is shown that the fast gain recovery of QCLs promotes two multimode regimes in QCLs: One is spatial hole burning (SHB), and the other one is related to the Risken-Nummedal-Graham-Haken (RNGH) instability predicted in the sixties. A model that can account for coherent phenomena, a saturable absorber and SHB is developed and studied in detail both analytically and numerically. A wide variety of experimental data on multimode regimes is presented. Lasers with narrow active region and/or with metal coating on the sides tend to develop a splitting in the spectrum, approximately equal to twice the Rabi frequency. It is proposed that this behavior stems from the presence of a saturable absorber, which can result from a Kerr lensing effect in the cavity. Lasers with a wide active region, which have weaker saturable absorber, do not exhibit a Rabi splitting, and their multimode regime is governed by SHB. This experimental phenomenology is well explained by our theoretical model.

List of papers submitted or published that acknowledge ARO support during this reporting period. List the papers, including journal references, in the following categories:

(a) Papers published in peer-reviewed journals (N/A for none)

- M. Trocolli, S. Corzine, D. Bour, J. Zhu, O. Assayag, L. Diehl, B.G. Lee, G. Höfler and F. Capasso, Electr. Lett. 41, 1059, (2005)
- L. Diehl, D. Bour, S. Corzine, J. Zhu, G. Höfler, B.G. Lee, C.Y. Wang, M. Trocolli and F. Capasso, Appl. Phys. Lett. 88, 041102, (2006).
- L. Diehl, D. Bour, S. Corzine, J. Zhu, G. Höfler, M. Loncar, M. Trocolli and F. Capasso, Appl. Phys. Lett. 88, 201115 (2006)
- L. Diehl, D. Bour, S. Corzine, J. Zhu, G. Höfler, M. Loncar, M. Trocolli and F. Capasso, Appl. Phys. Lett., 89, 081101 (2006)
- C.Y. Wang, L. Diehl, A. Gordon, C. Jirauschek, F.X. Kärtner, A. Belyanin, D. Bour, S. Corzine, G. Höfler, M. Troccoli, J. Faist and F. Capasso, Phys. Rev. A. 75, 31804 (2007)

Number of Papers published in peer-reviewed journals: 5.00

(b) Papers published in non-peer-reviewed journals or in conference proceedings (N/A for none)

Number of Papers published in non peer-reviewed journals: 0.00

(c) Presentations

C.Y. Wang et al., "Coherent Instabilities and self-pulsations in Qauntum Cascade Lasers" Quantum Electronics and Laser Science conference QELs, Long Beach, California, USA 2006

A. Gordon et al., "Multimode dynamics and mode locking phenomena in Quantum Cascade Lasers", 2nd International Workshop on Quantum Cascade Lasers, Brindisi, Italy 2006

Number of Presentations: 2.00

Non Peer-Reviewed Conference Proceeding publications (other than abstracts):

Number of Non Peer-Reviewed Conference Proceeding publications (other than abstracts): 0

Peer-Reviewed Conference Proceeding publications (other than abstracts):

Number of Peer-Reviewed Conference Proceeding publications (other than abstracts): 0

(d) Manuscripts

Number of Manuscripts:

Number of Inventions:

Graduate Students

NAME	PERCENT_SUPPORTED
Elizabeth Smythe	0.33
Christine Wang	0.33
FTE Equivalent:	**0.66**
Total Number:	**2**

Names of Post Doctorates

NAME	PERCENT_SUPPORTED
Mariano Troccoli	0.12
Davide Iannuzzi	0.11
Laurent Diehl	0.08
Christian Jirauschek	0.25
Ariel Gordon	0.30
FTE Equivalent:	**0.86**
Total Number:	**5**

Names of Faculty Supported

NAME	PERCENT_SUPPORTED	National Academy Member
Federico Capasso	0.00	Yes
Franz Kaertner		No
FTE Equivalent:	**0.00**	
Total Number:	**2**	

Names of Under Graduate students supported

NAME	PERCENT_SUPPORTED
FTE Equivalent:	
Total Number:	

Student Metrics

This section only applies to graduating undergraduates supported by this agreement in this reporting period

The number of undergraduates funded by this agreement who graduated during this period:	0.00
The number of undergraduates funded by this agreement who graduated during this period with a degree in science, mathematics, engineering, or technology fields:.....	0.00
The number of undergraduates funded by your agreement who graduated during this period and will continue to pursue a graduate or Ph.D. degree in science, mathematics, engineering, or technology fields:.....	0.00
Number of graduating undergraduates who achieved a 3.5 GPA to 4.0 (4.0 max scale):	0.00
Number of graduating undergraduates funded by a DoD funded Center of Excellence grant for Education, Research and Engineering:	0.00
The number of undergraduates funded by your agreement who graduated during this period and intend to work for the Department of Defense	0.00
The number of undergraduates funded by your agreement who graduated during this period and will receive scholarships or fellowships for further studies in science, mathematics, engineering or technology fields:	0.00

Names of Personnel receiving masters degrees

NAME

Total Number:

Names of personnel receiving PHDs

NAME

Total Number:

Names of other research staff

NAME	PERCENT_SUPPORTED

FTE Equivalent:

Total Number:

Sub Contractors (DD882)

Inventions (DD882)

Modelocking and coherent instabilities in Quantum Cascade lasers

Federico Capasso
School of Engineering and Applied Sciences, Harvard University, Cambridge, Massachusetts 02138, USA
August 23, 2007

Table of content:

1. Introduction
2. Prior work on multimode regime in Quantum Cascade Lasers
3. Maxwell-Bloch equations in a Fabry-Perot cavity
4. Ring cavity
5. Fabry-Perot cavity
6. Experimental results: ridge lasers
7. Experimental results: buried heterostructure lasers
8. Temperature effects
9. Conclusions
10. Aknowledgments

Appendix A
Appendix B
Bibliography
Publications

1. Introduction

This report describes in detail the activity of Prof. Capasso (Harvard University, responsible for the experimental part) and Prof. F.X. Kaertner (MIT, responsible for the modeling part) and covers the entire work performed throughout the duration of the U.S. Army Research Office Grant No. W911NF-04-1-0253.
Many physical mechanisms can drive a laser from a single-mode to a multi-mode regime. Common examples are spatial and spectral hole burning (SHB), saturable absorption, and self-phase modulation [1,2,3]. Understanding these mechanisms is of key importance to laser science and technology, whether one is interested in single-mode behavior or in a particular multi-mode operation such as mode locking.
The multimode regimes listed above are well understood and documented both theoretically and experimentally, in many types of lasers. However the understanding of multimode regimes in quantum cascade lasers (QCLs) is still in its infancy, as these lasers were only demonstrated in 1994 [4], and studies of their multimode regimes

commenced even more recently [5,6,7,8].
As it was shown recently [9] that multimode dynamics in QCLs are different from that of more common lasers. This is mainly due to the unusually fast gain recovery of QCLs, which occurs on a picosecond scale. While a saturable absorber triggers mode locking in lasers with slow gain recovery (relative to the roundtrip time), in lasers with fast gain recovery a saturable absorber triggers a mechanism similar to the Risken-Nummedal-Graham-Haken (RNGH) instability [10,11]. While in standard semiconductor lasers carrier diffusion eliminates spatial hole burning, in QCLs the gain recovery process is faster than carrier diffusion, and spatial hole burning is dominant.
This paper presents a detailed study of multimode regimes in QCLs. The results of Ref. [9] are substantiated and extended. The first part of the paper is theoretical and the second one is experimental. In the theoretical section, the laser Maxwell-Bloch equations are introduced and analyzed for both ring laser cavity and a Fabry-Perot cavity. This way one can study the interplay of coherent phenomena and spatial hole burning. A saturable absorber is added to the model as well. The model is studied analytically and numerically. The stability region of a continuous wave (CW) solution is found. It is shown that in a ring cavity, the presence of a saturable absorber lowers the threshold of the RNGH instability from about nine times above laser threshold to arbitrarily low above laser threshold, depending on the strength of the absorber. However, the nature of the instability remains the same: the population inversion begins to oscillate at the Rabi frequency, modulating the gain in the laser. The result is sidebands around the original CW mode, separated from it by roughly the Rabi frequency. A Rabi splitting in the spectrum is the primary signature of the RNGH instability.
It is then shown that the ring-cavity Maxwell-Bloch model with a saturable absorber can explain the Rabi splitting and the lowering of the threshold, but cannot explain a key feature in the experimental spectra. The latter exhibit two relatively equal groups of modes with a gap in between, whereas the ring-cavity Maxwell-Bloch model predicts a large central mode in the spectrum with two sidebands. In view of this discrepancy, the Maxwell-Bloch equations were extended to include coupling between counter-propagating modes in a Fabry-Perot cavity, which is of course a more adequate model for QCLs. This model takes into account the development of SHB. The inclusion of SHB generates theoretical spectra with a Rabi splitting and without a central peak in the spectrum, in agreement with experiments.
After presenting the theoretical results, a thorough study of the experimental phenomenology is presented. It is shown that QCLs with narrower active regions tend to exhibit a more pronounced Rabi splitting than lasers with wider active regions. Lasers with a wider active region tend to exhibit multimode spectra that are governed by SHB. The explanation we propose to this behavior is that narrow QCLs have a stronger saturable absorption effect than wider ones as a result of a Kerr-lensing effect [3,5]. In this case a nonlinear index enhancement in the waveguide core gives rise to an increased overlap of the transverse laser mode with an active region and a reduced overlap with lossy sidewalls, leading to an additional enhancement of the saturable absorption. The idea of saturable absorption by Kerr-lensing is further supported by the fact that QCLs with metal coating on the sides of the ridge have a stronger RNGH behavior than lasers without metal coating: The metal coating enhances saturable losses originated from Kerr-lensing.
In the last part of the paper, the temperature dependence of the multimode behavior in QCLs is studied experimentally. It is found that at higher temperature the multimode behavior tends to be governed by the RNGH instability, whereas at lower temperatures

it is governed by SHB. This behavior can be explained by the fact that at higher temperatures hot carriers populate more states in the injector superlattice, creating aditional quasi-resonant absorption transitions between ground and excited minibands. This leads to an additional saturable absorption of laser radiation.
This paper is organized as follows: Section 2 gives a brief survey of prior work on multimode regimes in QCLs, Sections 3-5 study theoretically the Maxwell-Bloch equations in a ring cavity and a Fabry-Perot cavity, Sections 6-8 summarize the experimental study, and Section 9 is a brief summary.
Note that most of the Quantum Cascade Lasers (QCLs) investigated during this project were grown by Dave Bour of Agilent Technologies. This fruitful collaboration with industry has led to the publication of several articles (see for example References [28] and [29] and the papers attached after Appendix A and B). The wafers were grown by metal organic vapor phase epitaxy (MOVPE), a crystal growth technique fitting the requirements of large-scale production. The material quality and the performance in continuous mode were shown to be comparable to or better than that of state-of-the-art QCLs grown by the standard deposition technique for these devices, namely molecular beam epitaxy or MBE.

2. Prior work on multimode regimes in QCLs

Multimode regimes in QCLs were observed in a series of recent works [5,6,7,8]. In Ref. [5], for example, it was observed that at a certain pumping current above lasing threshold, QCLs cease to operate in CW and develop a multimode regime. This multimode regime was characterized by a broadband optical spectrum and a narrow (less than 100 kHz) radio frequency (RF) beat note in the power spectrum.
The narrow beatnote, whose width is $1/10^5$ of the central frequency, shows that the waveform of the electric field circulating in the laser cavity was stable over approximately 10^5 roundtrips. In other words, the phase relationships between the longitudinal modes were stable for about 10^5 roundtrips. The modes were therefore locked. However in order to characterize the waveform which is circulating in the laser and to see if it is indeed an isolated pulse, as in traditional mode locking, one has to apply pulse characterization techniques, such as second order autocorrelation.
At the time when the experiment in Ref. [5] was performed, no second-order autocorrelation apparatus was available. However second harmonic generation from QCLs [6] provide some information for pulse characterization. This measurement shows an increase by more than a factor of 5 in the second harmonic signal as the multimode behavior sets in. This increase indicates that the duty cycle of the pulses was roughly 5. Since the number of modes in the spectrum is more than 5, we conclude that not all the modes were locked into a pulse. Without better pulse characterization data, one can infer that the laser could have had more than one pulse per roundtrip.
It should also be noted that traditional mode locking, with a single pulse per roundtrip, requires that the gain recovery time be longer than the cavity roundtrip [3]. In QCLs this condition is violated, and therefore according to the existing theory one cannot expect mode locking with a single pulse per roundtrip in QCLs. One can expect multiple pulses per roundtrip.
In view of the above, one can see that the nature of various multimode regimes in QCLs requires further elucidation. This is the main goal of the present work.

3. Maxwell-Bloch equations in a Fabry-Perot cavity

In this section we derive the Maxwell-Bloch equations in a Fabry-Perot cavity. We model the gain medium of QCLs as a two level system, described by the Bloch equations

$$\dot{\rho}_{ab} = \mathrm{i}\omega\rho_{ab} + \mathrm{i}\frac{\mu E}{\hbar}\Delta - \frac{\rho_{ab}}{T_2}, \quad (1)$$

$$\dot{\Delta} = -2\mathrm{i}\frac{\mu E}{\hbar}(\rho^*_{ab} - \rho_{ab}) - \frac{\Delta_p - \Delta}{T_1} + D\frac{\partial^2\Delta}{\partial z^2} \quad (2)$$

where ρ_{ab} is the off-diagonal element of the density matrix, $\Delta \equiv \rho_{bb}-\rho_{aa}$ is the population inversion, ω and μ are the resonant frequency and the dipole matrix element of the lasing transition, T_1 and T_2 are the longitudinal and transverse relaxation times, and Δ_p is the steady-state inversion at E=0 which characterizes the pumping rate. The last term in Eq. (2) is added phenomenologically and accounts for spatial diffusion of the inversion due to carrier diffusion. D is the diffusion coefficient. E is the electric field, which is assumed to satisfy the wave equation

$$\partial_z^2 E - \frac{n^2}{c^2}\partial_t^2 E = \frac{N\Gamma\mu}{\epsilon_0 c^2}\partial_t^2(\rho_{ab} + \rho^*_{ab}). \quad (3)$$

N is the number of two-level systems per unit volume, which equals to the doping density multiplies the number of QCL stages. Γ is the overlap factor between the optical mode and the active region, and n is the background refractive index.

Eqs. (1-2) describe an open two-level system [41]: The total number of electrons in the system is not conserved, but rather can flow in and out of the system. In general the two levels, the upper one b and the lower one a, can have different relaxation times. In this situation Eq. (2) should be replaced by two equations, each with its own relaxation times. In QCLs indeed the upper and lower levels have different relaxation times. However we neglect this difference for the sake of simplicity and assign to them the same value T_1. The generalization of the model (1-2) to a model with two different relaxation time is straightforward, as also is the generalization to a model with more than two levels.

We now make the following set of Ansatz:

$$E(z,t) = \frac{1}{2}\left[E^*_+(z,t)e^{-(\mathrm{i}\omega t - kz)} + E_+(z,t)e^{\mathrm{i}(\omega t - kz)}\right] + \frac{1}{2}\left[E^*_-(z,t)e^{-(\mathrm{i}\omega t + kz)} + E_-(z,t)e^{\mathrm{i}(\omega t + kz)}\right] \quad (4)$$

$$\rho_{ab}(z,t) = \eta_+(z,t)e^{\mathrm{i}(\omega t - kz)} + \eta_-(z,t)e^{\mathrm{i}(\omega t + kz)} \quad (5)$$

$$\Delta(z,t) = \Delta_0(z,t) + \Delta_2(z,t)e^{2ikz} + \Delta^*_2(z,t)e^{-2ikz}, \quad (6)$$

where $k \equiv \omega\, n/c$. $E_\pm$, $\eta_\pm$, Δ_0 and Δ_2 are assumed to vary slowly varying in time and space, on the scale defined by ω and k respectively. The quantities with a + (-) subscript represent waves traveling to the positive (negative) z direction. Eq. (7) allows taking SHB into account, Δ_2 being the envelope of the inversion grating. Note that Eq. (7) can be extended by adding terms proportional to e^{4ikz}, e^{6ikz} etc. Neglecting these terms means that higher spatial frequencies on the inversion are neglected. Due to the nonlinearity of the gain medium such frequencies can appear if the gain is heavily saturated, but they are neglected in our analysis for the sake of simplicity and since the pumping in our system is never much higher than the laser threshold.

Substituting Eqs. (4-7) into Eqs. (1-3) and making the slowly-varying envelope approximation, we obtain the following set of equations:

$$\frac{n}{c}\partial_t E_\pm = \mp\partial_z E_\pm - \mathrm{i}\frac{kN\mu\Gamma}{2\epsilon_0 n^2}\eta_\pm - \frac{1}{2}\ell(E_+,E_-)E_\pm \quad (7)$$

$$\partial_t \eta_\pm = \frac{\mathrm{i}\mu}{2\hbar}(\Delta_0 E_\pm + \Delta_2^\pm E_\mp) - \frac{\eta_\pm}{T_2} \quad (8)$$

$$\partial_t \Delta_0 = \frac{\Delta_p - \Delta_0}{T_1} + \frac{\mathrm{i}\mu}{\hbar}(E_+^\star \eta_+ + E_-^\star \eta_- - c.c.) \quad (9)$$

$$\partial_t \Delta_2^\pm = \pm\mathrm{i}\frac{\mu}{\hbar}(E_+^\star \eta_- - \eta_+^\star E_-) - \frac{\Delta_2^\pm}{T_1} - 4k^2 D\Delta_2^\pm \quad (10)$$

where we have introduced the notation $\Delta_2^+ \equiv \Delta_2$, $\Delta_2^- \equiv \Delta_2^*$ in order that Eqs. (8-11) can be written more compactly. The last term in Eq. (8) has been added, and represents loss. The loss ℓ is allowed to depend on the field to represent phenomena such as optical saturation.

In QCLs the laser cavity is formed by the two interfaces between the semiconductor medium and the outside air, one located at z=0, and the other one at z=L. L is the length of the cavity. At each interface the Fresnel reflection law dictates the following relations:

$$E_-(L,t) = \frac{n-1}{n+1}E_+(L,t) \quad (11)$$

$$E_+(0,t) = \frac{n-1}{n+1}E_-(0,t) \quad (12)$$

In what follows we study analytically and numerically the model introduced in this section. We begin with a simplified case, namely the standard Maxwell-Bloch equation in a ring cavity. In addition to briefly reviewing known results about the RNGH instability, we study the effect of a saturable absorber on the latter.

4. Ring cavity

In this section we consider a ring cavity, where SHB does not exist because standing waves cannot form. The aim is to understand the interplay of coherent effects and a saturable absorber alone, before further complications due to SHB come in. We shall see that without SHB, the qualitative agreement between theory and the experiments on QCLs is not complete. After introducing SHB in the next section, the agreement is much more satisfactory.

4.1. The RNGH instability with a saturable absorber

Dropping all the quantities with a '-' subscript from Eqs. (8-11), one arrives at the standard Maxwell-Bloch equations, with a saturable absorber added.

$$\frac{n}{c}\partial_t E = -\partial_z E - \frac{\mathrm{i}\mu\eta}{\hbar\ell_0\Delta_{\mathrm{th}}} - \frac{1}{2}(\ell_0 - \gamma|E|^2)E \quad (13)$$

$$\partial_t \eta = \frac{\mathrm{i}\mu}{2\hbar}\Delta E - \frac{\eta}{T_2} \quad (14)$$

$$\partial_t \Delta = \frac{\Delta_p - \Delta}{T_1} + \frac{\mathrm{i}\mu}{\hbar}(E^\star \eta - c.c.). \quad (15)$$

The saturable absorber is approximated to the lowest order in E, and is characterized by γ, which is often referred to as the self amplitude modulation coefficient. l_0 is the linear

loss. Δ_{th} is the lasing threshold value of Δ_p for $\gamma = 0$, given by:

$$\Delta_{\rm th}^{-1} = \frac{kN\mu^2\Gamma T_2}{2\hbar\ell_0\epsilon_0 n^2}. \qquad (16)$$

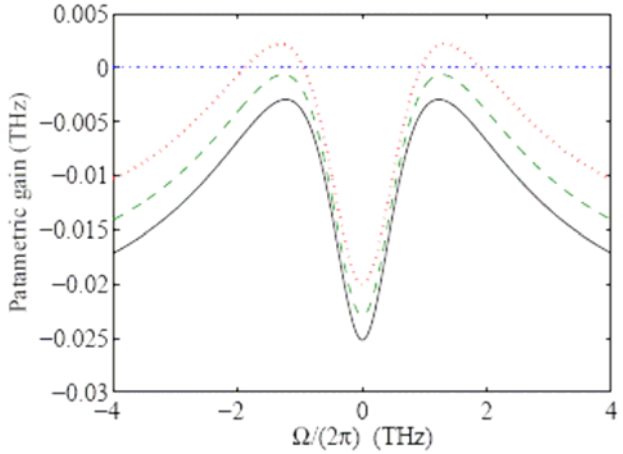

1. $g(\Omega)$ **for** $p=2$ **and the parameters in Table I, apart from** γ**. The latter is** $\gamma=0$ **(solid),** $\gamma = 10^{-9}\,cm/V^2$ **(dashed) and** $\gamma = 2\times10^{-9}\,cm/V^2$ **(dotted).**

Linear stability analysis of Eqs. (14-16) can be carried out. The gain of a perturbation at the frequency Ω (relative to the resonance frequency ω) is approximately given by

$$\begin{aligned} g(\Omega) &= -\frac{c}{2n}\mathrm{Re}\left[\ell_0\frac{(\Omega T_1+\mathrm{i})\Omega T_2 - 2(p-1)}{(\Omega T_1+\mathrm{i})(\Omega T_2+\mathrm{i})-(p-1)}+\right. \\ &+ \left.\frac{\gamma\hbar^2(p-1)}{\mu^2 T_1 T_2}\frac{(\Omega T_1+\mathrm{i})(3\Omega T_2+2\mathrm{i})-4(p-1)}{(\Omega T_1+\mathrm{i})(\Omega T_2+\mathrm{i})-p+1}\right] \end{aligned} \qquad (17)$$

The approximations made in the derivation of Eq. (18) mainly include assuming that the photon lifetime in the empty cavity is much longer than T_1 and T_2. This approximation is excellent for QCLs. p is the pumping above lasing threshold (for $\gamma=0$):

$$p \equiv \frac{\Delta_p}{\Delta_{\rm th}}. \qquad (18)$$

Figure 1 shows $g(\Omega)$ for different values of γ at $p=2$. The parameters used in all examples in this paper, unless specified otherwise, are given in Table I. The effect of γ is to increase $g(\Omega)$ more or less uniformly across the frequency domain. In particular, it can bring $g(\Omega)$ above zero, thereby triggering an instability, even when the laser is not pumped as high above threshold. The reason why a saturable absorber lowers the RNGH threshold is that a saturable absorber itself always favors a multimode regime to a single mode one. It introduces a frequency-independent parametric gain. The latter is added to the RNGH parametric gain from Fig. 1, bringing it above threshold. Note, however, that the instability still starts by developing Rabi sidebands around the CW lasing frequency. In this sense, it can be interpreted as a modified version of the original RNGH instability, rather than as a modulation instability caused by the saturable absorber alone.

Quantity	Symbol	Value
Gain recovery time	T_1	0.5 ps
Dephasing time	T_2	0.067 ps
Linear cavity loss	ℓ_0	5 cm^{-1}
Transition dipole element	μ	2.54 nm$\times e$
Background refractive index	n	3
Cavity length	L	3 mm
Saturable absorber coefficient	γ	$10^{-8}\frac{cm}{V^2}$

1. The parameters used in all calculations and simulations in this paper, unless indicated otherwise.

The dependence of the threshold for instability on γ is shown in Fig. 2. For γ=0 we recover the standard RNGH instability, which occurs at the pumping of slightly above 9 times above lasing threshold. For $\gamma \to \infty$ the instability threshold approaches the lasing threshold.

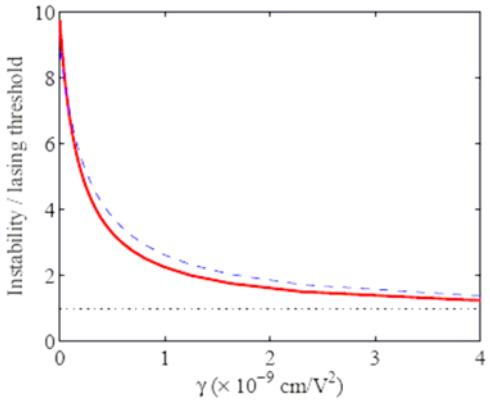

2. The pumping ratio p at which the RNGH instability sets in as function of the saturable absorber coefficient γ. Solid line – exact result from linear stability analysis. Dashed line – approximate result (Eq. (23)). The parameters, apart from γ, are given in Table I.

The results in Fig. 1 and Fig. 2 were obtained from numerical solutions of the algebraic equations involved in the stability analysis. Since even the approximate expression of g(Ω) (Eq. (18)) is not very simple, it is useful to derive some approximate simple expressions for the properties of the instability. Here we only give the results.

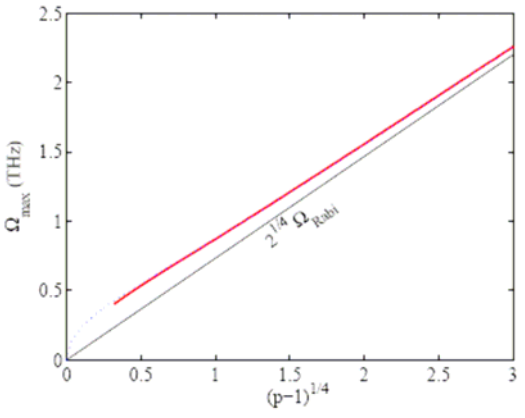

3. Ω_{max} as function of the pumping. Thick line: exact, dotted line: Eq. (21). The parameters are from Table I with the only difference that γ=0

g(Ω) (e. g. in Fig. 1) has a local minimum at Ω=0, and peaks at approximately

$$|\Omega_{\max}| = \Omega_{\mathrm{Rabi}} \sqrt[4]{\frac{2p}{p-1}}. \qquad (19)$$

The position of the peak depends weakly on γ within the parameter range of interest to our system. Note that for γ=0 one has

$$\Omega_{\mathrm{Rabi}} = \sqrt{\frac{p-1}{T_1 T_2}}. \qquad (20)$$

The dependence of $|\Omega_{\max}|$ on p is shown in Fig. 3.

The instability threshold is approximately given by

$$p_{\mathrm{th}} = 1 + 8\left[4\left(\frac{\hbar^2\gamma}{\mu^2 T_2^2 \ell_0}\right)^2 + 12\frac{\hbar^2\gamma}{\mu^2 T_2^2 \ell_0} + 1\right]^{-1}. \qquad (21)$$

Figure 2 shows that Eq. (23) fairly well approximates the exact threshold condition.

4.2. Numerical results

The linear stability analysis given above can only find the threshold condition, and does not describe the behavior of the laser above the point of instability. Here we therefore present the results of a numerical solution of Eqs. (14-16).

According to Ref. [30], the state of the laser can change either discontinuously or continuously at the RNGH instability threshold. In the language of phase transitions, this would be a first or second order phase transition respectively. The criterion that determines the order of the transition involves the laser cavity length, but has not been given explicitly in the literature known to us.

According to the numerical simulations, for the parameters corresponding to our QCLs, including the saturable absorber, the transition is continuous (second order). Below the instability threshold the lasing is CW, and as the threshold is crossed, the Rabi sidebands around the central CW mode grow continuously. This behavior is demonstrated in Fig.4. Note that standard mode locking, with a saturable absorber and slow gain recovery, is a discontinuous (first-order) transition [43,44].

The spectra in Fig.4 have two groups of modes separated by roughly twice the Rabi frequency. In this respect they resemble the experimental spectra. However they have a strong CW peak in between, a feature which is not shared by the experimental spectra. As we show in the next section, in a Fabry-Perot cavity with SHB, the central CW peak disappears.

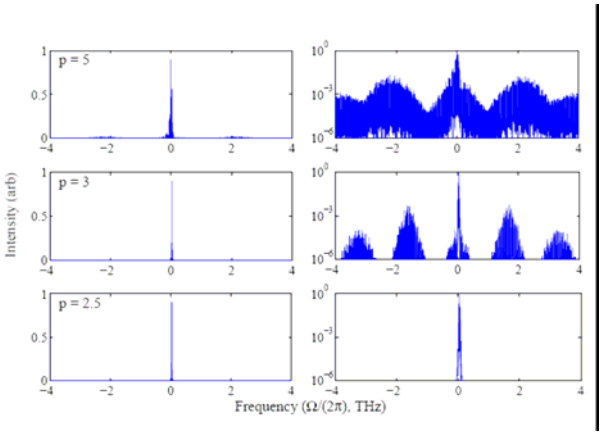

4. Spectra obtained from a numerical solution of the Maxwell-Bloch Eqs. (13-15). The parameters are given in Table I.

5. Fabry-Perot cavity

Spatial hole burning is associated with Δ_2 in Eq. (11). Intuitively, Δ_2 is the amplitude of the grating that couples the two propagation directions in the laser. The parameter that controls the strength of SHB is D: in the limit of $D\rightarrow\infty$, Δ_2 approaches zero. In order to better understand the interplay between SHB and the RNGH instability, we present now the results of analytical and numerical studies of Eqs. (8-11). We start with linear stability analysis and here we only give the results.

Before proceeding, we define the lifetime of the gain grating T_g as seen in Eq. 11, as

$$T_g^{-1} = T_1^{-1} + 4k^2 D.$$

T_g is the parameter that determines the strength of spatial hole burning. T_g can therefore range from zero (no SHB) to T_1 (strongest of SHB). The diffusion coefficient D can be estimated from the Einstein relation. In AlInAs-InGaAs heterostructures, the electron mobility can reach as high as 16000 cm^2/sec/V at room temperature [45]. Thus one has 400 cm^2/sec, $k=3.7*10^4$ cm^{-1}, which roughly corresponds to a vacuum wavelength of 5 μm, we obtain $4k^2D \approx 2$ THz. With $T_1^{-1} \approx 2THz$ we find that $T_g \approx 0.25$ ps. Note that the mobility used here was relatively high, the wavelength was on the short side of the scale and room temperature was taken. Therefore in reality T_g is closer to T_1. It therefore follows that due to the fast gain recovery of QCLs, carrier diffusion does not eliminate spatial hole burning. This is in contrast with diode lasers.

5.1. Linear stability analysis

Linear stability analysis of Eqs. (8-11) gives two families of unstable modes. One is associated with the RNGH instability, and the other one – with spatial hole burning. The first family is very similar to the case of a ring cavity studied earlier, with small differences. The second one can also be derived and the result is shown in Fig. 5.

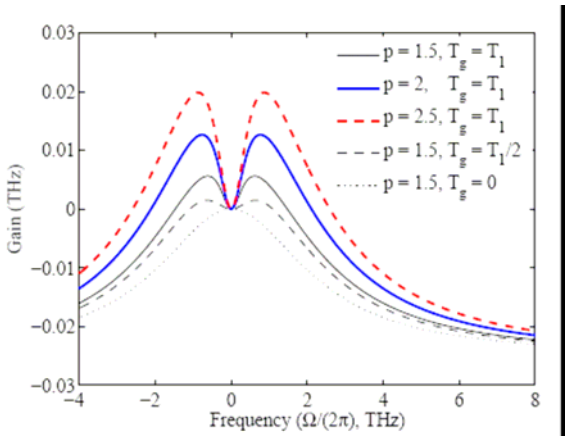

5. g(Ω) of the perturbation, associated with spatial hole burning. p and T_g corresponding to every curve is denoted in the legend.

Figure 4 shows the gain of a perturbation around a CW solution. The shorter is T_g and the smaller is the pumping, the smaller is the gain of the instability. For parameters typical to our QCLs, the SHB instability occurs a few percents above lasing threshold. The gain curve in Fig. 5 exhibits two peaks and a dip at Ω=0. For $T_2 \ll T_1$ and $p-1 \ll 1$, the location of the peaks is given by:

$$\Omega_{\max}^2 \approx \frac{1}{T_1}\sqrt{\frac{p-1}{3T_1T_2}}. \qquad (22)$$

Note that Eq. (22) gives a smaller frequency than Eq. (19). In addition, the splitting in Fig. 5 scales like the square root of the Rabi frequency. CW is destabilized when the cavity admits a mode for which g(Ω) in Fig. 5 is positive.

5.2. Numerical results

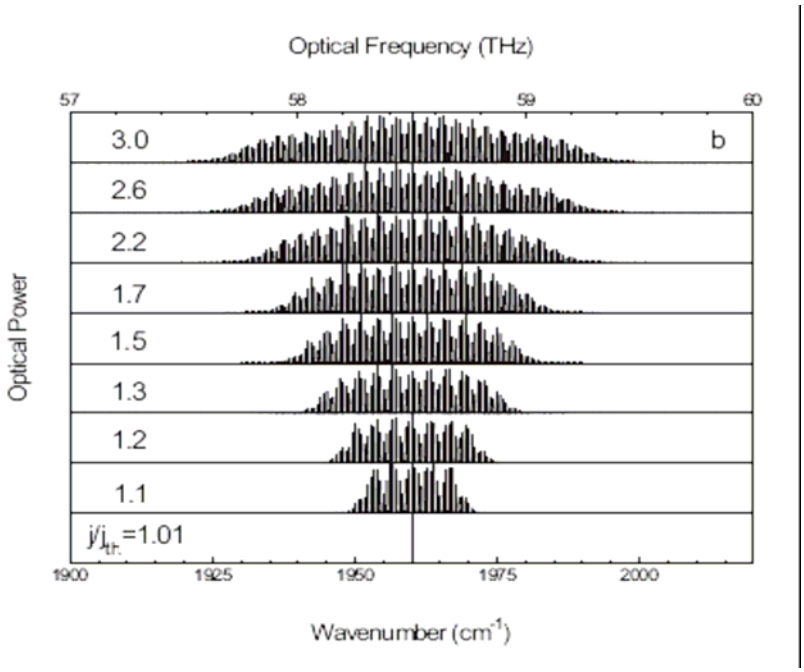

6. Results of numerical simulations of the spectra based on the Maxwell-Bloch equations including a saturable absorber and spatial hole burning for different values of the current density normalized to the threshold value.

The moment CW is destabilized, studying Eqs. (7-10) requires a numerical simulation. The results of such a simulation are shown in Fig. 5. The parameters are given in Table I, with the only difference that $\gamma=0$ was used.

Fig. 6 shows a clear pattern in the spectrum. This pattern appears only after very long averaging (order of a microsecond) of the spectrum. Such averaging is appropriate, since similar averaging occurs when the spectra are measured. The pattern depends on T_2 and ℓ_0, but very weakly depends on T_1. A similar pattern occurs in the experimental spectra. However we were not able to understand its origin.

5.3. Saturable absorber

The combined effect of SHB and a saturable absorber is demonstrated in Fig. 7. One can observe two effects. First is spectral broadening due to SHB, similarly to Fig. 6. Second however is the appearance of a splitting in the spectrum. This splitting is roughly equal to twice the Rabi frequency. Note however that contrary to a ring laser, in a Fabry-Perot laser "the Rabi frequency" is not a well defined concept. Since a standing wave is formed in the cavity, the electric field and thus the Rabi frequency depend on the position in the cavity. This dependence is even stronger when the the mirrors have a relatively low reflection coefficient, since the field amplitude even more strongly depends on position.

In the previous section we saw that a saturable absorber lowers the threshold of the RNGH instability. Here we see that SHB suppresses the central peak seen in Fig.4 and

replaces it by a minimum in the spectrum. In the next sections we see that Fig. 7 agrees well with experimentally measured spectra, at least for devices where the RNGH behavior was dominant.

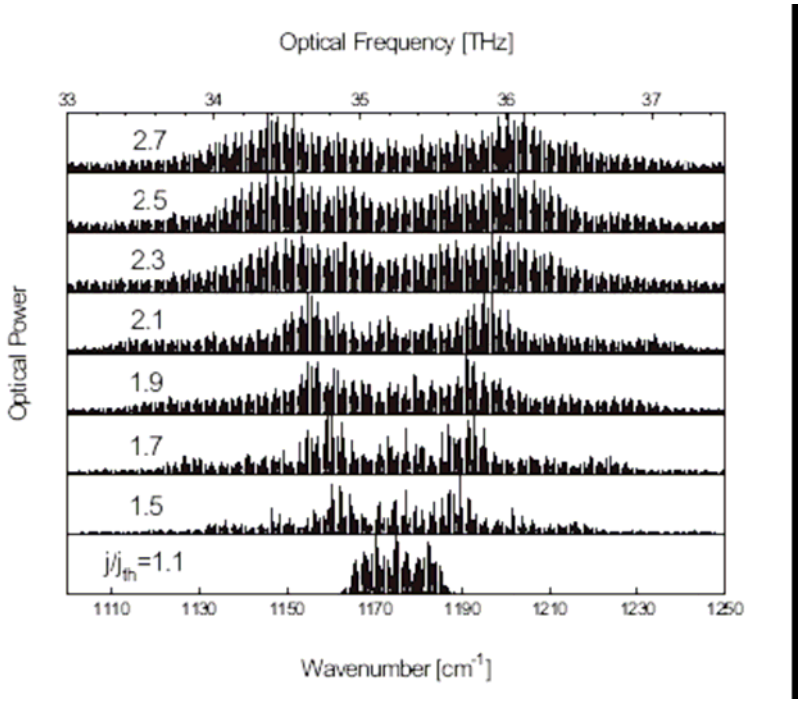

7. Results of numerical simulations of the spectra based on the Maxwell-Bloch equations including a saturable absorber and spatial hole burning for different values of the current density normalized to the threshold value.

6. Experimental results: ridge lasers

We first study the multimode regimes in standard ridge QCLs, in which the sidewalls of the laser ridges are covered by a thick layer of electrically plated gold contact. This acts as a Kerr-lens type saturable absorber; see Fig. 8 for a typical laser cross section. The Kerr-lensing mechanism is explained in detail in Appendix B. The active region of the samples tested is based on a three-quantum-well design emitting at a wavelength $\lambda \sim 8\mu m$ [31]. The wafer was grown by metalorganic vapor phase epitaxy (MOVPE). Fig. 9 a shows the voltage-current (V-I) and light-current (L-I) characteristics of a 10 μm wide laser operated in CW at 200K, and b shows the corresponding optical spectra. The laser was cleaved into a 2 mm long bar and soldered with Indium onto a copper heat sink. The optical power was measured by an OPHIR thermal head powermeter with a collection efficiency of nearly 100%. The spectra were measured by a Nicolet Fourier transform infrared spectrometer (FTIR) equipped with a deuterated triglycine sulphate (DTGS) detector.

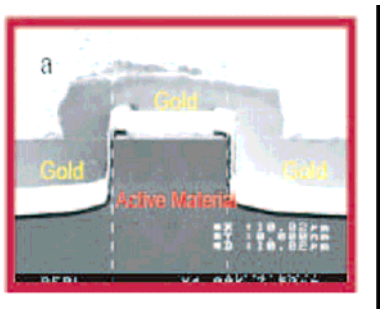

8. Scanning electron microscope (SEM) image of the cross section of a 10 [Trial mode]m wide ridge QC laser.

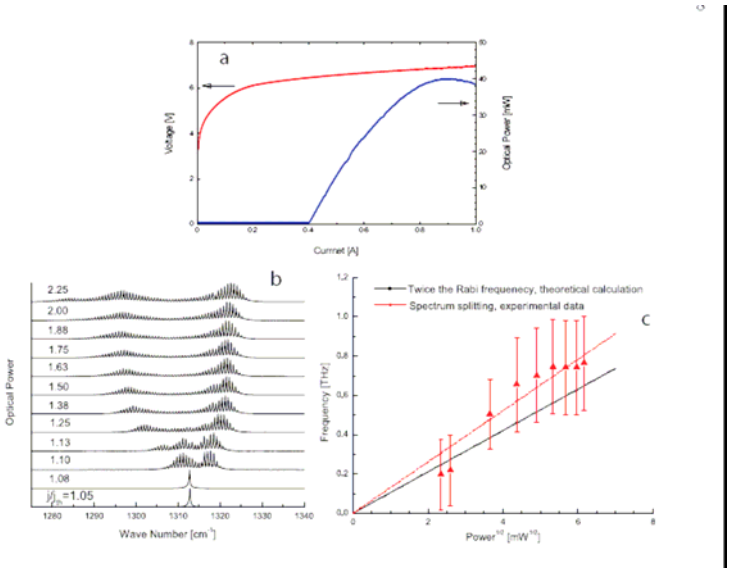

9. (a) V-I and LI curves and (b) optical spectra vs. pumping ratio (j/j_{th}) above threshold obtained in CW at 200K of a 10 μm wide ridge laser emitting at 8μm. (c) Spectral splitting and twice the Rabi frequency vs. square root of output power collected from a single facet. The different quantities reported on the graph were deduced from the experimental data show in (b). The dashed line is the least-square linear fit of the data.

As shown in Fig. 9 b, the laser spectrum is single mode close to laser threshold. It broadens and splits into two separated humps as the pumping current increases. The separation between the two peaks of the two humps increases linearly with the square root of the collected output power from one facet, as shown in Fig. 9 c. The Rabi angular frequency can be calculated from the collected output power, using the formula $\Omega_{Rabi} \equiv \mu E / \hbar$, where μ is the electron charge times the matrix element of the laser transition (=1.9 nm for this particular device). I_{ave} is the average intracavity intensity in the gain region, which can be derived from the measured output power [32]. For all values of intensity corresponding to the spectra reported in Fig. 9 b, $\Omega_{Rabi} / 2\pi$ was calculated, multiplied by a factor of two and then added to Fig. 9 c (solid line). Reasonably good agreement is found between the experimental splitting and twice the estimated Rabi frequency. The error bars of the spectrum splittings come from the uncertainty in determining the exact position of the peaks, which is the

full-width-at-half-maximum (FWHM) of the humps. As mentioned previously in the theoretical section, the RNGH instability predicts that large intracavity intensity will result in parametric gain at frequencies detuned from the maximum of the gain curve by the Rabi frequency. The measured spectra thus show strong indication of the RNGH instability in ridge QCLs.

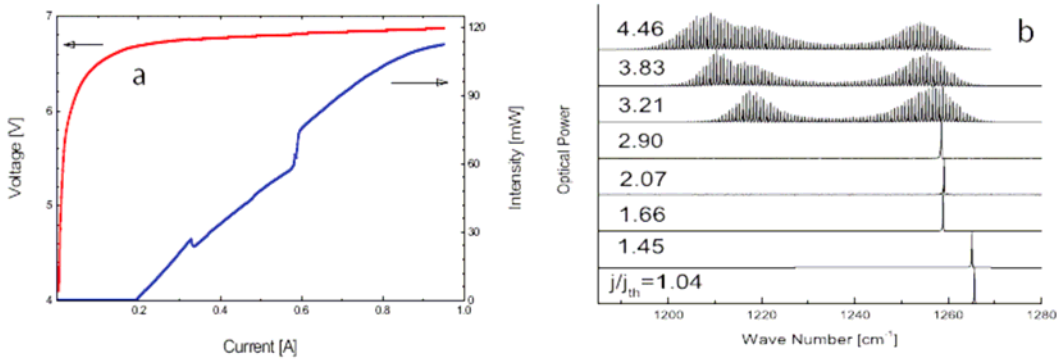

9. (a) **V-I and LI curves and (b) optical spectra vs. pumping ratio (j/j_{th}) above obtained from a 10 μm wide ridge QCL operated in CW at 77K emitting at 8 μm Note that mode hoping occurs while there is a jump in the LI curve.**

The lowering of the RNGH instability threshold in our QCLs is due to the presence of a saturable absorber. This phenomenon is demonstrated analytically in the theoretical section. Such a saturable absorption mechanism in our experiments is likely to come from Kerr-lensing, caused by a nonlinear (i.e. intensity dependent) refractive index n_2I in the active region [5]. As the light intensity increases, the mode becomes more confined in the plane transverse to the propagation direction, and the net gain it undergoes also increases. The reason is twofold: First, the mode overlaps more with the active region, leading to a larger modal gain (this mechanism is often called "soft Kerr-lensing"). Second, the overlap with the metal contacts is reduced, leading to smaller losses. A detailed analysis is given in Appendix B.

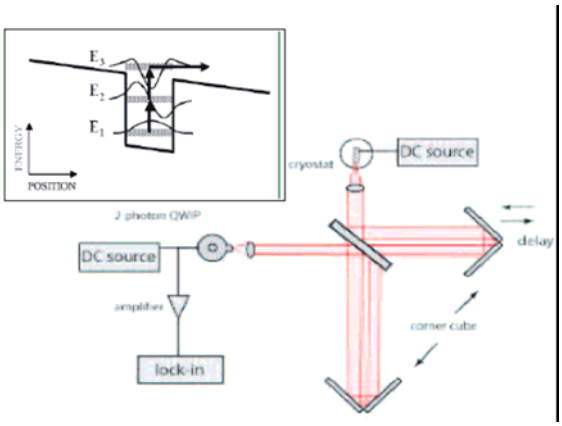

11. The experimental setup of a two-photon autocorrelation measurement. (Inset) Conduction band diagram of the two-photon QWIP showing three equidistant energy levels.

The same RNGH splitting in spectra is observed in many different devices, from wafers grown by both molecular beam epitaxy (MBE) and MOVPE. Fig. 10 shows the spectra

of a laser fabricated from a MBE-grown wafer with the same active region design as in Fig. 7, taken in continuous wave at 77K. The spectrum starts from single mode close to the laser threshold, and the mode hops at a pumping ratio of j/j_{th} =1.66, where there is a correponding kink in the L-I curve at 330mA. At 590mA, there is another kink in the L-I curve, relating to the broadening of the spectrum and a hop in the mode center. Mode-hopping and its relationship to kinks in the L-I curves are common phenomena in semiconductor lasers [33,34,35], but its cause in QC lasers is not yet studied and is beyond the focus of this paper. After the spectrum broadens, it forms two separated humps whose peaks shift apart with increased optical power, similar to the MOVPE-grown case.

Characterization of our ultra-short pulses was done using the standard method of second-harmonic interferometric autocorrelation. The setup is based on a Michelson interferometer in which the input beam is split into two and one of them is delayed by τ.Once recombined, the two pulses are sent colinearly first into a nonlinear crystal, and then a filter, which allows only the second-harmonic generation (SHG) component to be detected. One can test if it is an isolated pulse from the ratio between the interference maximum and the background (see Appendix A). The pulse duration can also be determined. However, due to the extremely low SHG conversion efficiency of mid-IR in nonlinear crystals, the conventional setup is not feasible. To overcome this problem, we use a two-photon quantum well infrared photodetector (QWIP) which converts the second-harmonic signal electrically [36,37] instead of using a nonlinear crystal plus a linear detector. The energy diagram of one period of the multi quantum well detector under bias is shown in the inset of Fig. 11. The first three electronic states are nearly equidistant in energy. When electrons in the doped quantum wells absorb two photons simultaneously and the detector is biased (1-3 V), a photocurrent is generated and the signal can be detected by use of a pre-amplifier and a lock-in amplifier. This experimental setup is diagramed in Fig. 11. The second-order autocorrelation trace of the MBE-grown device mentioned above is shown in Fig. 12. Interference fringes are observed when the delay time from one arm of the autocorrelator is equal to the multiples of the cavity roundtrip time. The ratio between the maximum of the interference fringes and the background is smaller than 8, and the autocorrelation trace has some features between the cavity roundtrip times, indicating that the multimode regime observed in this device is not stable mode locking with a single pulse per roundtrip. The meaning of the autocorrelation traces are discussed in Appendix A, and simulated traces are given therein.

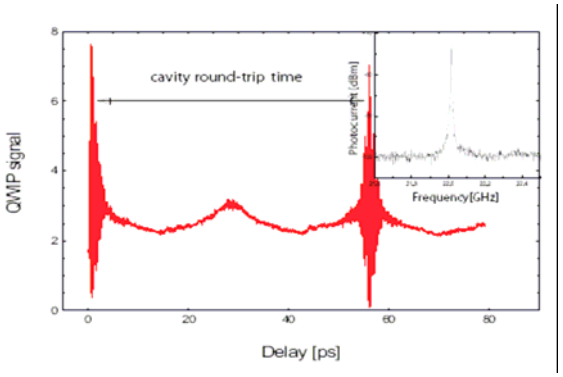

12. A second-order autocorrelation trace of a 8 μm wavelength ridge QC laser (wafer # 2743) under the condition of RNGH instability. (Inset) Microwave spectrum of photocurrent generated by a similar laser (wafer # 2721) under the condition of RNGH instability (measured with a 68 kHz resolution bandwidth).

In addition to second-order autocorrelation, the microwave spectrum of the laser output was also measured with an ultrafast QWIP [38] whose bandwidth is 52 GHz. The laser output is sent directly to the ultrafast QWIP, and the resulting photocurrentis displayed in a spectrum analyzer. Fig. 12 shows the beat note signal of the MOVPE-grown sample at pump current 800 mA at 77K. A steady peak with FWHM of 13 MHz at 22.01 GHz, which corresponds to the cavity round trip frequency of the 2 mm long laser (background refractive index n=3), is observed on the spectrum analyzer. It indicates a modulation of the laser output at the cavity roundtrip frequency, and thus at least partial phase locking between the longitudinal modes: The phase relationships between the modes are stable for about 10^3 roundtrips.

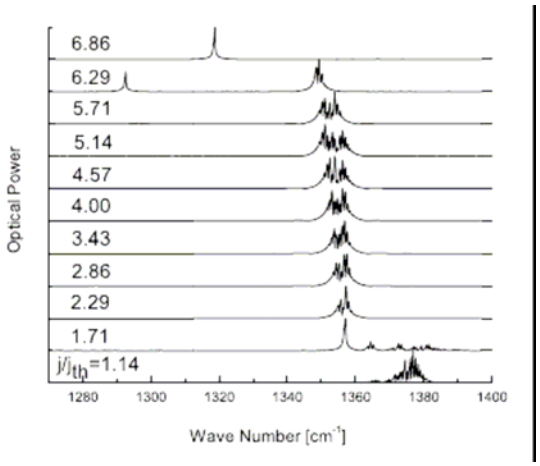

13. Optical spectra vs. pumping ratio ([Trial mode]) above threshold obtained in CW at 77K with a 15 µm wide ridge laser emitting at 8 µm (wafer# 2721).

As the ridge width is increased, the RNGH instability and the Rabi splitting in the spectrum are suppressed. Fig. 13 shows the spectra of a device processed from the same wafer as the one in Fig. 9, with the difference of its ridge width being increased to 15 µm. The spectra do not broaden much even at very high pumping current, and do not show the Rabi splitting. As discussed in Appendix B, the effect of Kerr-lensing decreases significantly when the active region width is increased. Thus, this is a strong evidence that the saturable absorption needed for lowering the RNGH threshold is provided by the Kerr-lensing mechanism.

7. Experimental results: Buried heterostructure lasers

The second type of lasers we have tested are the so-called buried heterostructure lasers, in which an insulating Fe-doped InP layer is regrown after etching of the ridges. A thick layer of electrically plated gold is deposited on top of the ridges as top contact layer after the InP regrowth . Figure 14 shows the cross section of such a laser.

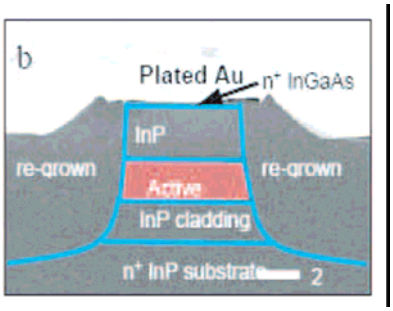

14. SEM image of the cross section of a buried heterostructure QC laser.

The active region of the buried heterostructure lasers tested is based on the four-quantum-well design, which relies on a double phonon resonance to achieve population inversion [39]. Fig. 15 a shows the V-I and L-I characteristics of a laser with active region width of 3 μm and wavelength 8.38 μm operated in CW at room temperature, and b shows its optical spectra. The spectra show Rabi splitting similar to the ridge laser case, indicating the RNGH instability in this narrow buried heterostructure laser. The spectral splitting and twice the Rabi frequency are plotted against the square root of the collected output power in Fig. 15 b. A good agreement is found between the experimental splitting and twice the calculated Rabi frequency.

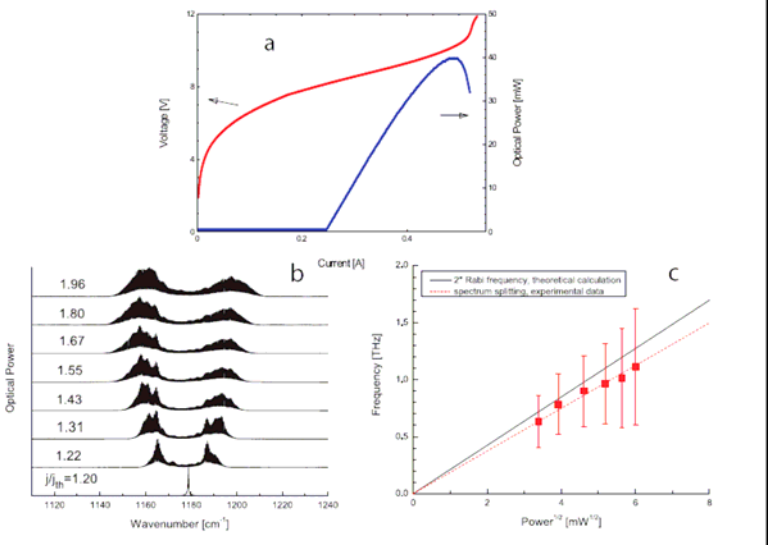

15. (a) V-I and LI curves and (b) optical spectra vs. pumping ratio (j/j_{th}) above threshold obtained in CW at 300K of a 3 μm wide ridge laser emitting at 8μm. (c) Spectral splitting and twice the Rabi frequency vs. square root of output power collected from a single facet. The different quantities reported on the graph were deduced from the experimental data show in (b). The dashed line is the least-square linear fit of the data.

The second-order autocorrelation trace of the device when it is pumped five times above threshold at 80K is shown in Fig. 16. The ratio between the maximum of the interference fringes and the background is close to 8 to 3, similar to the ridge laser case. In addition, there are smaller interference fringes within one cavity roundtrip period. Both features indicate no stable pulsation from the laser (see Appendix A). The microwave spectrum of the laser output shows a steady peak with FWHM of 700 kHz at 15.018 GHz. This is shown in the inset of Fig. 16.

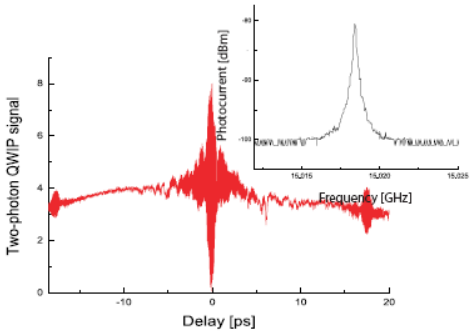

16. A second-order autocorrelation trace of a 8 μm wavelength buried heterostructure QC laser (wafer # 3251) under the condition of RNGH instability. (Inset) Microwave spectrum of the photocurrent generated by the same laser (measured with a 68 kHz resolution bandwidth).

As in the ridge laser case, the lowering of the threshold of RNGH instability can also be attributed to the Kerr-lens type saturable absorption. In order to better support this idea experimentally, the spectra from another device processed from the same wafer as in Fig. 15 but with a wider active region (7.5 μm) are measured. Two-dimensional waveguide simulations indicate a much weaker Kerr-lensing effect in these QCLs, due to the much larger ratio of active region width to wavelength (see Appendix B). The measured optical spectra obtained at 300K in CW mode are shown in Fig. 17 a. The envelopes of the spectra consist of multiple peaks whose separation is independent of the pumping current. The spectral signatures qualitatively agree with the numerical simulations in a Fabry-Perot cavity without a saturable absorber (γ =0) (Fig. 6).

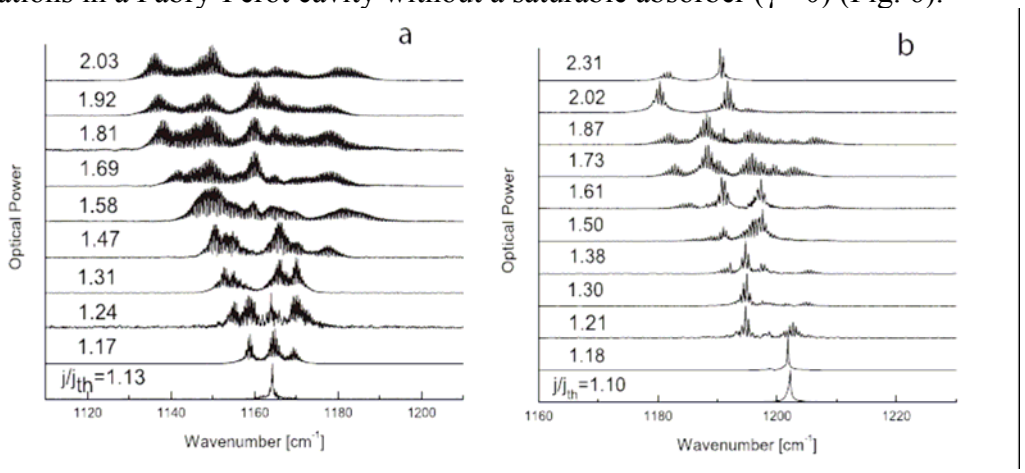

17. Optical spectra vs. pumping ratio (j/j_{th}) above threshold obtained in CW at 300K with (a) a 7.5 μm wide and (b) a 7.5 μm buried heterostructure lasers emitting at 8μm.

Further increasing the active region width tends to suppress both the instabilities caused by RNGH and spatial hole burning. Fig. 17 b shows the spectra of a device also processed from the same wafer but with an even wider active region (10 μm) at 77K. The spectra do not broaden much even at very high pumping currents, as in the ridge laser case. Since both RNGH instability and SHB stem from nonlinear effects, they are suppressed when the intensity of the field in the cavity is lower. Moreover, when the active region width increases, higher transverse modes are excited. Different transverse modes have different propagation constants β, and thus form different gain gratings which tend to wash out the effect of spatial hole burning.

8. Temperature effects

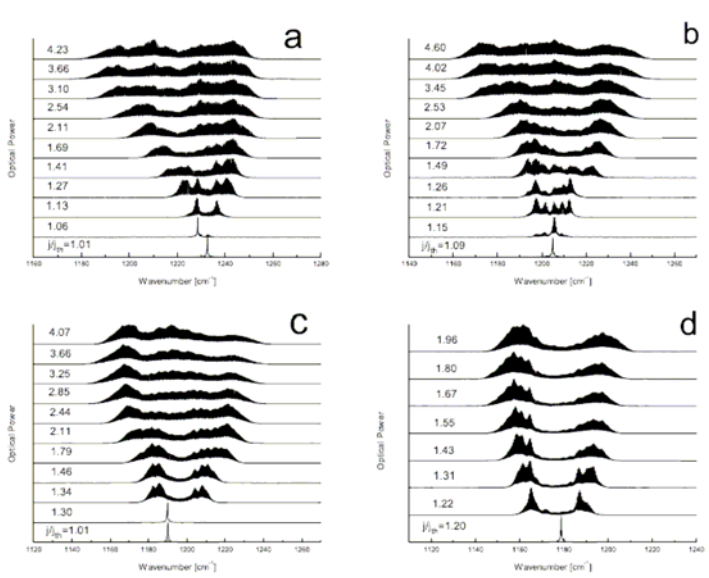

18. Optical spectra vs. pumping ratio (j/j_{th}) above threshold obtained in CW of a buried heterostructure emitting at 8.38μm at different temperatures: (a) 80K, (b) 150K, (c) 200K and (d) 300K.

Temperature also plays an important role in the shape of the spectrum. To illustrate this point, we now present the spectra at different temperatures for the λ=8.38 μm buried heterostructure laser with 3 μm active region width (the same as in Fig. 15).

From the spectra in Fig. 18, it is clear that at lower temperatures the spectra are dominated by spatial hole burning, showing multiple peaks independent of pumping and no significant Rabi splitting. As the temperature increases, the Rabi splitting becomes more evident and finally the RNGH instability takes over.

Intuitively, the effect of the temperature on the nature of the multimode regime in QCLs seems to come from carrier diffusion. The lifetime of the gain grating T_g is defined as $T_g^{-1} = T_1^{-1} + 4k^2 D$. The diffusion coefficient D of the gain grating is proportional to the temperature, $D = \mu k_B T / q$, where μ here is the carrier mobility, k_B is the Boltzmann's constant, T is the temperature and q is the carrier charge. Therefore at higher temperature carrier diffusion would reduce spatial hole burning and thus reveal the RNGH instability. However, with a mobility of 16000 $cm^2/sec/V$ and $k=2.25*10^4$ cm^{-1} (which corresonds to a vacuum wavelength of 8.38μm), $4k^2D \approx 0.2$ THz at 77K and $4k^2D \approx 0.8$ THz at 300K, both significantly smaller than $T_1^{-1} \approx 0.6$ THz at 77K and $T_1^{-1} \approx 2$ THz at 300K. Thus, carrier diffusion is unlikely to be the reason for the temperature dependence. Although the temperature effect is not entirely understood to us at this point, one possiblity is temperature-dependent saturable absorption. The QCL injector consists of many energy levels which can be thermally populated. It is not surprising that if any two higher levels in the injector are closely resonant with the laser transition, and that they will form a two-level saturable absorber.Therefore in this case saturable absorption is stronger at higher temperature and makes the RNGH more easily observable.

9. Conclusion

This paper provides a thorough account of different multimode regimes in QCLs. It was found that two key mechanisms which govern the multimode regimes in QCLs are a coherent instability similar to the RNGH instability, and spatial hole burning. Both mechanisms are enhanced due to the large dipole moment μ of the laser transition, which results in the unusually fast gain recovery in QCLs: The RNGH instability is enhanced because the Rabi frequency scales as μ, and therefore the Rabi splitting can be resolved by the comb of modes supported by the cavity. SHB is enhanced because carrier diffusion is slower than the gain recovery, and thus leaves the gain grating intact.

Due to the fast gain recovery, conventional mode locking, with one pulse per roundtrip, is suppressed. In order to achieve conventional mode locking in QCLs, one needs to design a QCL with a slower gain recovery, such that T_1 becomes longer than or comparable to the cavity roundtrip. Efforts in this direction are currently underway.

10. Acknowledgements

Support from the U.S. Army Research Laboratory and the U.S. Army Research Office under grant number W911NF-04-1-0253 is gratefully acknowledged. Part of the device processing was done at the Center for Nanoscale Systems (CNS) at Harvard University. Harvard-CNS is a member of the National Nanotechnology Infrastructure Network (NNIN)

Appendix A. Interferometric autocorrelation

If we write the electric field as function of time as $E(t)e^{i\omega t}$, the two-photon interferometric autocorrelation is given by

$$I(\tau) = \int_{-\infty}^{\infty} |E(t+\tau)e^{\mathrm{i}\omega\tau} + E(t)|^4 dt =$$

$$= \int_{-\infty}^{\infty} \left[|E(t+\tau)|^4 + |E(t)|^4 + 4|E(t+\tau)E(t)|^2\right] dt +$$

$$+ \ 2\left[\int_{-\infty}^{\infty} dt|E(t)|^2 E^*(t)E(t+\tau)e^{\mathrm{i}\omega\tau} + c.c.\right] +$$

$$+ \ 2\left[\int_{-\infty}^{\infty} dt|E(t+\tau)|^2 E^*(t)E(t+\tau)e^{\mathrm{i}\omega\tau} + c.c.\right] +$$

$$+ \left[\int_{-\infty}^{\infty} dt(E(t+\tau)E^*(t)e^{2\mathrm{i}\omega\tau})^2 + c.c.\right]. \qquad \text{(B1)}$$

We define the background as

$$I_b = 2\int_{-\infty}^{\infty} |E(t)|^4 dt. \qquad \text{(B2)}$$

From Eq. (65) one can see that $I(0)=8I_b$. We now assume that E(t) is an isolated pulse, and for the sake of simplicity we assume that E(t) is nonzero only over an interval T**.** Then for $\tau > T$ all terms in Eq. (65) which include both t and $t+\tau$ vanish. Therefore $I(\tau>T)=I_b$**.** In other words, for a pulse one has

$$\frac{I(0)}{I(\tau > T)} = 8. \qquad \text{(B3)}$$

Now let us assume that E(t) is a complex stationary random process whose phase at each point in time is uniformly distributed over the interval $[0, 2\pi]$**.** Let us assume for simplicity that there is T such that for $\tau>T$**,** E(t) and $E(t+\tau)$ are statistically independent. One can see that the mean value of the third, the fourth and the fifth line of Eq. (65) vanish. The second line of Eq. (65) equals $3I_b$. We therefore obtain that for a random process

$$\frac{I(0)}{I(\tau > T)} = \frac{8}{3}. \qquad \text{(B4)}$$

The ratio between the peak and the background in the autocorrelation function is therefore 8:1 for an isolated pulse, that is when the phases of all modes are all zero, and 8:3 for modes with completely random phases.

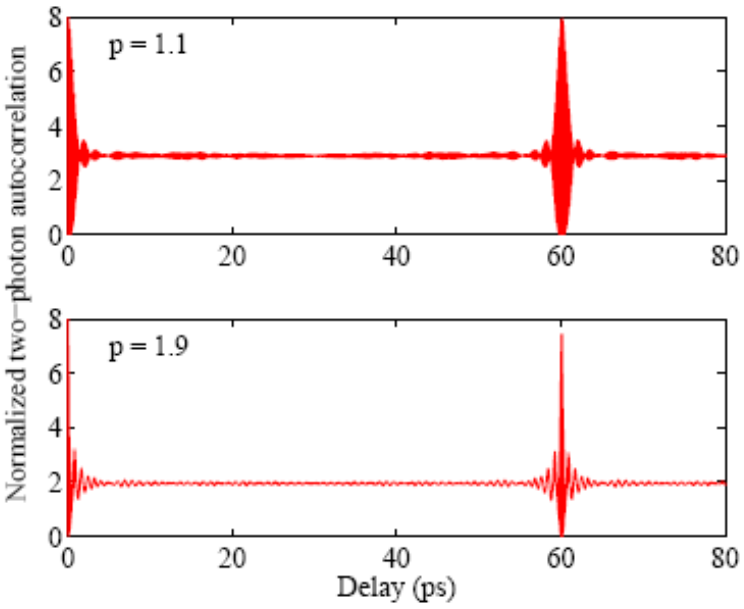

19. Simulated interferometric autocorrelation, corresponding to the same parameters as in Fig. 7. The value of p is denoted at each plot.

Fig.19 shows simulated interferometric autocorrelation traces for the same parameters as in Fig. 6. For p=1 the phases of the modes are random, and the peak to background ratio is 8:3. When the saturable absorber is absent, $\gamma=0$, the ratio in the autocorrelation is also 8:3. When the pumping is higher (Fig. 19 below), the saturable absorber induces some phase relationships between the modes, and the peak to background ratio is about 8:2. Note that in the autocorrelation in Fig. 12, the ratio is slightly greater than 8:3. The autocorrelation also has a nontrivial structure, with a peak at half the cavity roundtrip time. We were not able to reproduce this structure in the simulations.

Appendix B. Kerr lensing in QCLs

This section elaborates on the analysis of the Kerr lensing effect (including soft Kerr lensing) in QCLs. The mechanism of Kerr lensing can be understood as follows: above lasing threshold, there is net gain in the active region which compensates the mirror losses. Assuming a nonlinear refractive index $\Delta n_{NL} = n_2 \cdot I$ in the active region, it causes self focusing of the transverse mode, which results in a net increase in the modal gain due to an increased overlap with the active region and a decreased overlap with lossy waveguide cladding. A stronger intensity leads to stronger Kerr lensing, thus forming an intensity-dependent saturable absorber.

The active region width is expected to play an important role in the Kerr lensing effect. The narrower the active region, the less confined is the transverse mode, which results in a bigger increase of the modal gain due to Kerr lensing. Therefore the saturable absorber coefficient γ is expected to be larger in lasers with narrower active region.

We performed FDTD waveguide simulations using the commercial software BeamPROP. We simulated buried heterostructure QCLs (wafer # 3251) with various active region widths. The software allows us to assign complex refractive indices to each layer, and the effective modal index is calculated by the software. The detailed steps of our Kerr lensing simulation are as follows:

1. We first assign a net gain (i.e., a negative imaginary part of n_{active}) in the active region, making the total modal gain equal to the total mirror loss. In our case, given the reflectivity r=0.27 at our laser facets, a 3mm long laser hasa total mirror loss of 4 cm^{-1}.
2. We assign different values of $\Delta n_{NL} = n_2 \cdot I$ to the real part of n_{active}. After running the simulation, we get the net modal gain for each n_{NL}.
3. We plot the modal gain versus Δn_{NL}. For example, Fig. 20 shows the plots for 3 μm wide and 5 μm wide active regions.
4. In order to relate to our theoretical model, the change in modal gain is attributed entirely to change in modal losses.
5. The change in modal loss equals to $\gamma |E|^2$, which is also proportional to the intensity I Thus, from the slope of the plot of modal gain vs. $\Delta n_{NL} = n_2 \cdot I$,we can extract the ratio of γ/n_2.
6. For a given active region width, we choose the value of γ that brings the threshold of RNGH instability down close to our experimental data. Then we can determine the value of n_2 from the ratio of γ/n_2.
7. With the fixed value of n_2, we repeat the waveguide simulation with different active region widths and plot γ vs. the active region width.

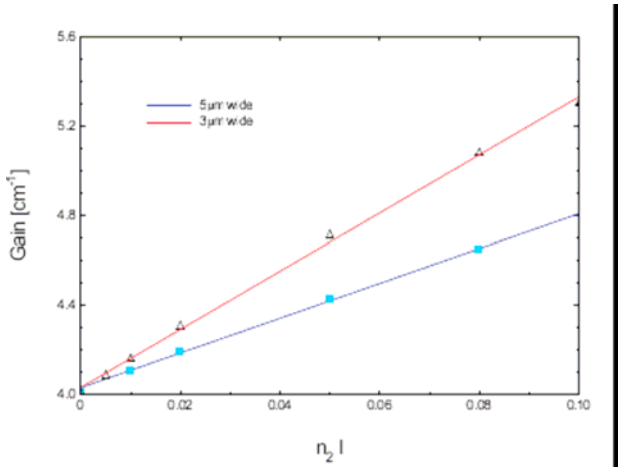

20. Simulation results of the modal gain vs. the nonlinear refractive index [Trial mode] for a 3μm wide and a 5μm wide active region in wafer # 3251.

For an active region width of 3 μm, the RNGH threshold is dramatically lowered from nine times the lasing threshold to less than twice the lasing threshold (see Fig. 11). From Fig. 2, the required γ is about $2*10^{-9}$ cm/V^2, from which we obtain that n_2 is about $2*10^{-8}$ cm^2/W. The estimated γ vs. active region width is plotted in Fig. 21. As the active region width increases, γ decreases, and when the active region is as wide as 7.5 μm, γ decreases to $1*10^{-9}$ cm/V^2**.** This pushes the RNGH instability threshold to above twice the lasing threhsold. This may explain why we see only instabilities resulting from spatial hole burning in wider buried heterostructure lasers (see Fig. 17).

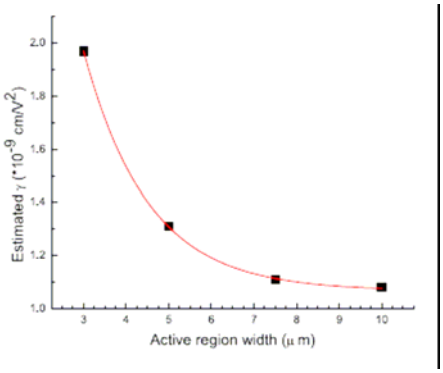

21. Simulation results of the saturable absorber coefficient γ vs. the active region width in wafer # 3251 assuming $n_2=2*10^{-8}$ cm^2/W.

For ridge lasers, the lossy gold contact on the sidewalls of the laser ridges will make the saturable absorber even stronger. This may explain the absence of spatial hole burning in ridge lasers.

There are several possibilities which might explain the origin of n_2 in the active region. First, the material we use has a thermal index change of $\Delta n/\Delta T = 1.55\times10^{-4}K^{-1}$, and when the laser is operating in CW, the active region usually heats up by tens of degrees. Second, the complex states in the injector can all contribute to both real and imaginary parts of $\chi^{(3)}$ at the laser wavelength, which results in both n_2 and γ. The latter effect should be enhanced with increasing temperature since electrons populate a larger amount of absorbing states at higher temperatures. Third, although not very significant, there is always bulk n_2 of the material.

Bilbliography:

[1] A. E. Siegman, *Lasers*, University Science Books, Mill Valley, CA (1986).
[2] A. Yariv, *Quantum Electronics*, **3rd** edition, John Wiley and Sons, New York (1989)
[3] H. A. Haus, IEEE J. Sel. Top. Quant. Electron. , 1173 (2000).
[4] J. Faist, F. Capasso, D. L. Sivco, C. Sirtori, A. L. Hutchinson, and A. Y. Cho, Science **264**, 553 (1994).
[5] R. Paiella *et al.,* Science **290**, 1739 (2000).
[6] A. Soibel, F. Capasso, C. Gmachl, M. L. Peabody, A. M. Sergent, R. Paiella, D. L. Sivco, A. Y. Cho, and H. C. Liu, IEEE J. Quantum Electron. **40** 197 (2004).
[7] A. Soibel, F. Capasso, C. Gmachl, M. L. Peabody, A. M. Sergent, R. Paiella, H. Y. Hwang, D. L. Sivco, A. Y. Cho, H. C. Liu, C. Jirauschek, and F. X. Kärtner, IEEE J. Quantum Electron. **40** 844 (2004).
[8] R. Paiella, F. Capasso, C. Gmachl, H. Y. Hwang, D. L. Sivco, A. L. Hutchinson, and A. Y. Cho, Appl. Phys. Lett. **75**, 2536 (1999)
[9] C. Y. Wang, L. Diehl, A. Gordon, C. Jirauschek, F. X. Kärtner, A. Belyanin, D. Bour, S. Corzine, G. Höfler, M. Troccoli, J. Faist, and F. Capasso, Phys. Rev. A. **75**, 31802 (2007).
[10] H. Risken and K. Nummedal, J. Appl. Phys. **39**, 4662 (1968).
[11] P. Graham and H. Haken, Z. phys. **213**, 420 (1968).
[12] A.Z. Grasiuk and A.N. Oraevsky, Proc. VI Int. Congr. on Microwave Tubes, Scheveningen, Holland, 1962.
[13] H. Haken, *Synergetics*, Springer, New York (1983).
[14] Ya. I. Khanin, *Principles of laser dynamics*. North-Holland, Amsterdam (1996).
[15] H. Haken, Phys. Lett. A , 77 (1975).
[16] L. Allen and J. H. Eberly, *Optical resonance and two level atoms*, Dover, New York (1987).
[17] C.O. Weiss and J. Brock, Phys. Rev. Lett. , 2804 (1986).
[18] L. W. Hillman, J. Krasiński, R. W. Boyd, and C. R. Stroud, Jr., Phys. Rev. Lett. **52**, 1605 (1984).
[19] E. H. M. Hogenboom, W. Klische, C. O. Weiss, and A. Godone, Phys. Rev. Lett. **55**, 2571 (1985).
[20] E. M. Pessina, G. Bonfrate, F. Fontana, and L. A. Lugiato, Phys. Rev. A **56**, 4086-4093 (1997).
[21] T. Voigt, M.O. Lenz, F. Mitschke, E. Roldán, and G.J. de Valcŕcel, Appl. Phys. B **79**, 175 (2004).
[22] H. Fu and H. Haken, J. Opt. Soc. Am. B **5**, 899 (1988).
[23] E. Roldán, G. J. de Valcárcel, J. F. Urchueguia, and J. M. Guerra, J. Opt. Soc. Am. B **20**, 816 (2003).
[24] R. Paiella *et al.*, Appl. Phys. Lett. **79**, 2526 (2001).
[25] F. Capasso, C. Gmachl, D. L. Sivco, and A. Y. Cho, Physics Today, **55**, 34 (2002).
[26] T. Norris, private communication.
[27] F. Capasso *et al.*, IEEE J. Quantum Electron. **38**, 511 (2002).
[28] L. Diehl *et al.*, Appl. Phys. Lett. **88**, 201115 (2006).

[29] L. Diehl *et al.*, Appl. Phys. Lett., **89**, 081101 (2006)
[30] H. Haken and H. Ohno, Opt. Commun. **26**, 117 (1978).
[31] C. Gmachl, *et al.*, Appl. Phys. Lett. **72**, 3130 (1998).
[32] The ratio between the intracavity power and the collected output power can be derived from the reflective coefficients of the laser facets and the collection efficiency of the power meter. Ω_{Rabi} can be derived from the intracavity power given the overlap factor of the laser mode with the laser active region.
[33] M. Ohtsu, Y. Otsuka and Y. Teramachi, Appl. Phys. Lett. **46**, 108 (1985)
[34] N. Chinone *et al.*, IEEE J. Quantum Electron. **21**, 1264 (1985)
[35] M. Ohtsu *et al.*, IEEE J. Qantum Electron. **22**, 535 (1986)
[36] A. Zavriyev *et al.*, Opt. Lett. **20**, 1886 (1995)
[37] T. Maier *et al.*, Appl. Phys. Lett. **84**, 5162 (2004)
[38] For a general review of ultrafast QWIPs, see H. C. Liu *et al.*, IEEE Circuits & Devices Magazine, November 2003, p.9-16.
[39] M. Beck, *et al.*, Science **295**, 301 (2002).
[40] The main contribution to the error bars is due to the width of the two peaks in the specra.
[41] R. W. Boyd, *Nonlinear optics*, second ed., Academic Press, London (2003).
[42] F. Salin, J. Squier, and M. Piché, Opt. Lett. **16**, 1674 (1991).
[43] A. Gordon and B. Fischer, Phys. Rev. Lett. **89**, 103901 (2002).
[44] A. Gordon, B. Vodonos, V. Smulakovsky, and B. Fischer, Opt. Express **11**, 3418 (2003)
[45] X. Wallart, B. Pinsard, and F. Mollot, J. Appl. Phys. **97**, 053706 (2005)

Pulsed- and continuous-mode operation at high temperature of strained quantum-cascade lasers grown by metalorganic vapor phase epitaxy

L. Diehl[a)]
Harvard University, Division of Engineering and Applied Science, Cruft Laboratory 310, 19 Oxford Street, Cambridge, Massachusetts 02138

D. Bour, S. Corzine, J. Zhu, and G. Höfler
Agilent Laboratories, Photonics and Electronics Research Laboratory, 3500 Deer Creek Road, Palo Alto, California 94304

B. G. Lee, C. Y. Wang, M. Troccoli, and F. Capasso
Harvard University, Division of Engineering and Applied Science, Cruft Laboratory 310, 19 Oxford Street, Cambridge, Massachusetts 02138

(Received 19 August 2005; accepted 23 November 2005; published online 23 January 2006)

We present the pulsed operation at room temperature of different strained InGaAs/AlInAs quantum-cascade lasers grown by low-pressure metalorganic vapor-phase epitaxy. Devices based on a bound-to-continuum transition design have threshold current densities in pulsed mode as low as 1.84 kA/cm^2 at 300 K. Identical lasers grown at higher rate (0.5 nm/s) also have threshold current densities lower than 2 kA/cm^2 at 300 K. Buried heterostructure lasers based on a double phonon resonance design were operated in continuous mode up to 280 K. Overall, the performance obtained from strained quantum cascade lasers deposited by metalorganic vapor-phase epitaxy are comparable with that of similar structures grown by molecular beam epitaxy. © *2006 American Institute of Physics*. [DOI: 10.1063/1.2166206]

Quantum cascade lasers (QCLs) are the light source of choice for many potential applications such as gas sensing in the midinfrared.[1] State-of-the-art QCLs have indeed demonstrated large tunability, low-threshold, and high-power in continuous mode (cw) at room temperature.[2,3] The devices which exhibit the best performance have been so far grown by molecular beam epitaxy (MBE). This fabrication technique provides several advantages, such as the ease to form abrupt interfaces, but is not suitable for low-cost, high throughput production. On the contrary, low-pressure metalorganic vapor-phase epitaxy (MOVPE) is a well-established technology fitting the requirements of large scale production, especially since high growth rates are possible.[4–6] However, it is still necessary to demonstrate that MOVPE- and MBE-grown QCLs can have similar performance particularly since the control of interface abruptness is more challenging by MOVPE. QCLs fabricated using the latter technique have already been operated recently at room-temperature in pulsed mode. The threshold current densities for these lattice-matched devices were low, i.e., between 2.4 and 3 kA/cm^2 at 300 K and the emission wavelength longer than 7.2 μm.[4,6] Structures at shorter wavelengths require in order to achieve high performance at room temperature, the use of strain-balanced material because of the large band discontinuity available.[7]

This letter reports on the fabrication of strained QC lasers grown by MOVPE working in pulsed mode above 320 K. Threshold current density as low as 1.84 kA/cm^2 at 300 K and characteristic temperature T_0 close to 200 K were obtained from devices based on a bound-to-continuum design. Another sample based on a double phonon resonance design worked in cw up to 280 K. More than 80 mW output power was delivered by the device in cw mode at 243 K.

Three strained QC structures were deposited on highly doped substrate by low pressure (76 Torr) MOVPE. The parameters were identical to those used for the growth of the lattice-matched QCLs reported in Refs. 5 and 6. The flows of triethylgallium and trimethylaluminium were simply adjusted to form the strained $In_{0.6}Ga_{0.4}As$ and $Al_{0.56}In_{0.44}As$ alloys. The active region of the first two samples investigated is based on a bound-to-continuum design previously reported by Blaser *et al.*[3] and was deposited at a slow (0.1 nm/s) and a fast (0.5 nm/s) rate. The doping in the injector was kept low (1×10^{17} cm^3) to limit the waveguide losses. Thirty stages were grown and embedded between 0.3-μm-thick InGaAs guiding layers doped 3×10^{16} cm^3, in addition to 3-μm-thick InP cladding layers doped 1×10^{17} cm^3. Step-graded 30-nm-thick InGaAsP layers were inserted at the InP–InGaAs interfaces to reduce series resistance. The growth ended with a 0.5-μm-thick InP layer doped 1×10^{19} cm^3 for plasmon-enhanced optical confinement and reduced losses, followed by highly doped contact layers. The deposition rate, except in the active region was kept constant at a value of 0.5 nm/s. The third structure studied in this letter replicates the lasers described in Refs. 8 and 9 based on a double phonon resonance design. Our sample comprises 30 stages and the waveguide is similar to the one described earlier.

Figure 1 shows the x-ray diffraction spectra of the two QCLs based on a bound-to-continuum design, together with the results of simulations. The comparison between the different patterns clearly shows very similar diffraction spectra, no noticeable degradation of the crystal quality as the growth rate changes and an excellent reproducibility of the structure

[a)]Electronic mail: ldiehl@deas.harvard.edu

 © 2006 American Institute of Physics
Downloaded 31 Jan 2006 to 128.103.60.225. Redistribution subject to AIP license or copyright, see http://apl.aip.org/apl/copyright.jsp

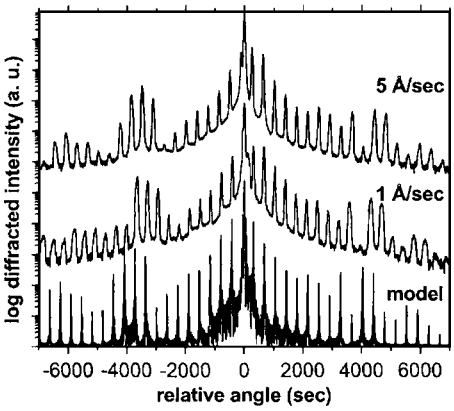

FIG. 1. Comparison between simulations and x-ray diffraction spectra of the fast- and slow-grown bound-to-continuum QCL measured along the (004) crystal direction. The curves are shifted for clarity.

from one run to the other. For both samples, the zeroth order peak due to the periodicity of the superlattice is very close to the InP substrate peak, which indicates only a slight lattice mismatch in the structures. The average length of the QC stages can be deduced from the different spectra. The period of the active region is 49.3 and 49.7 nm for the slow- and fast-grown structures, respectively, which is in both cases thinner than the targeted thickness (50.6 nm). This observation is consistent with the fact that the emission wavelength of our lasers is blueshifted with respect to the original design [4.98 μm vs 5.4 μm, see the inset of Fig. 2(a)].

Ridge waveguide lasers were fabricated using conventional processing techniques. The samples were cleaved manually, soldered ridge side-up with indium onto gold-plated copper heatsinks and finally wire bonded. After fabrication, the lasers were mounted into a temperature-controlled LN_2-cooled flow cryostat. Current pulses (163 ns) at a frequency of 92 kHz, corresponding to a duty cycle of 1.5%, were supplied to the lasers. For measurements in continuous mode, the devices were mounted on a Peltier cooler installed in a purged box. The light from the laser facet was collected by $f/1$ optics and sent either onto a calibrated thermopile detector for power measurements or into a Fourier-transform infrared spectrometer equipped with a deuterated triglycine sulphate detector for spectral characterization.

Figure 2(a) shows the voltage and the light-intensity versus current (*VI* and *LI*) curves of a 1.9-mm-long and 16-μm-wide laser fabricated from the slow-grown material. The maximum emitted peak power was 156 and 51 mW with a slope efficiency dP/dI equal to 564 and 380 mW/A at, respectively, 243 and 300 K. The inset of Fig. 2(a) shows typical spectra obtained close to threshold.

The threshold current density j_{th} measured in pulsed mode is plotted as function of temperature in Fig. 2(b) for the fast- and slow-grown samples. In both cases, the lasers worked at temperatures above 320 K and the characteristic temperature T_0, which describes the behavior of the threshold current versus temperature was close to 200 K. For the slow-grown device, j_{th} ranges from 1.39 to 2.07 kA/cm^2 between 243 and 320 K and is close to the values obtained in Ref. 3. In this letter indeed, a threshold current density of 1.38 kA/cm^2 was reported for a 3-mm-long device operated in continuous mode at a heatsink temperature T_{sink} of 243 K. The latter corresponds to a temperature in the active region $T_{act}=T_{sink}+T_{elec}\cdot R_{th}$ close to 266 K, given the electric power

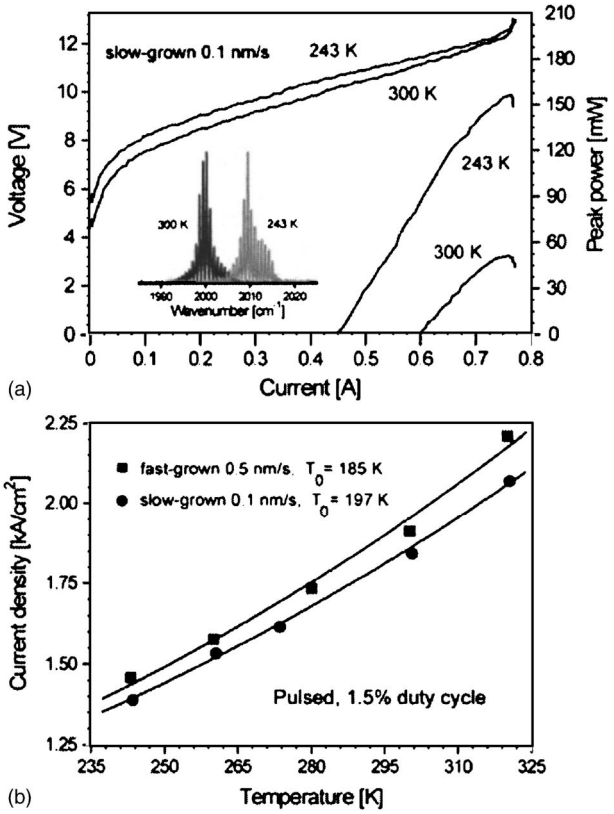

FIG. 2. Summary of the data obtained with the lasers based on a bound-to-continuum transition design in pulsed mode. (a) *VI*/*LI* curves and optical spectra close to threshold (inset) taken at 243 and 300 K with the slow grown sample. (b) Threshold current density vs temperature for the slow- and fast-grown QCLs. Note that the latter has a cavity length 31% longer than the slow-grown laser. The curves correspond to the usual exponential fit $j_{th}=j_0\exp(T/T_0)$.

P_{elec} of 3.75 W and the thermal resistance of R_{th} 6.3 K/W measured by Blaser *et al.* Assuming that heating effects are negligible in pulsed mode, we can expect for their device a pulsed threshold of 1.38 kA/cm^2 at about 266 K. This is only 15% lower than the threshold current density of the slow-grown QCL investigated in the present letter. This difference would be even smaller lasers of equal length were compared.

As shown in Fig. 2(b), the threshold current density of the fast-grown lasers is less than 2 kA/cm^2 up to 304 K and the characteristic temperature T_0 reaches 185 K. This result is remarkable given the high deposition rate (0.5 nm/s) used during the growth of the sample. However, the difference in terms of performance between the slow- and fast-grown QCLs is not negligible, although the curves in Fig. 2(b) suggest the contrary. It is due to the fact that the cavity length of the fast-grown QCL was longer (2.52 mm) than in the case of the slow-grown sample. If both lasers would have been cleaved in exactly 2-mm-long bars, the difference in threshold current density would be about 20% higher. Note that the measured slope efficiency is only 232 mW/A for the fast grown samples.

The QC sample based on a double phonon resonance design was processed into narrow-stripe buried heterostructure lasers. In this case, the active region is surrounded by insulating InP doped with Fe, lowering the thermal resistance of the device and allowing continuous wave operation at high temperatures. To reduce the thermal resistance even fur-

Downloaded 31 Jan 2006 to 128.103.60.225. Redistribution subject to AIP license or copyright, see http://apl.aip.org/apl/copyright.jsp

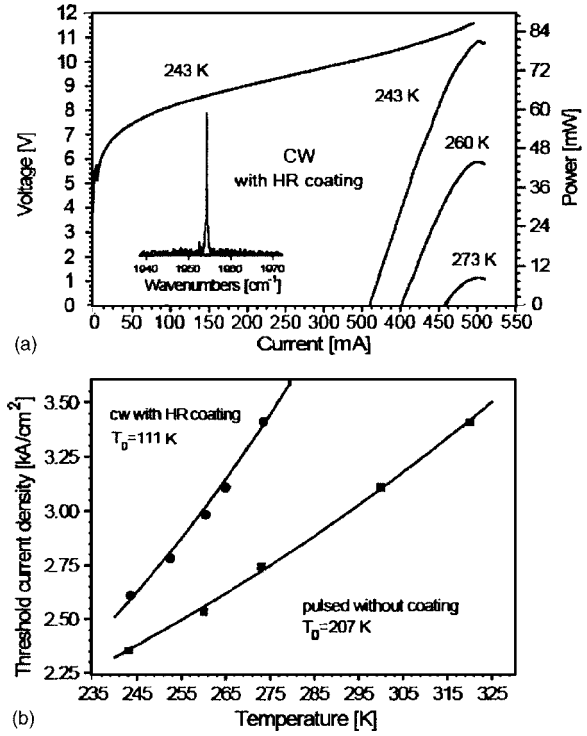

FIG. 3. Summary of the data obtained with the structure based on a four quantum wells transition design in pulsed and continuous mode. (a) *VI* and *LI* taken at different temperatures in continuous mode after the evaporation of a HR coating on the backfacet. The inset shows the optical spectra measured close to threshold at 243 K. (b) Threshold current density as a function of the heatsink temperature in pulsed and continuous mode, respectively without and with a high-reflection coating. The curves correspond to the usual exponential fit $j_{th}=j_0 \exp(T/T_0)$.

ther, a thick layer of gold was electroplated onto the usual Ti/Au top contact. The best results were obtained with a 7-μm-wide and 2-mm-long laser mounted junction-up, which operated at temperatures above 320 K in pulsed mode. The measured slope efficiency with a 1.5% duty cycle reached 636 mW/A at 243 K and 339 mW/A at 320 K. The device could be operated in continuous mode at 243 K. The temperature range accessible was, however, limited since the cw threshold current density (3.29 kA/cm^2 at 243 K) was fairly close to the injection current at which the roll-over of the output power takes place (3.74 kA/cm^2 at 243 K). The maximum intensity was 6.6 mW and the slope efficiency 172 mW/A. A high-reflection (HR) coating consisting of 175 nm Al_2O_3 and 30 nm Au was deposited on the backfacet of the laser and helped to reduce the cw threshold current density. The value of the latter dropped to 2.61 kA/cm^2 at 243 K and the maximum cw temperature operation of the laser increased up to 280 K. Figure 3(a) shows the cw *VI-LI* curves of the device after the evaporation of the HR coating. The intensity reached 81 mW (dP/dI=657 mW/A) at 243 K and was still 8 mW (dP/dI =257 mW/A) at 273 K. The inset of Fig. 3(a) shows a typical spectrum obtained if the laser is operated slightly above threshold in cw mode. At 243 K, the emission wavelength is 1954 cm^{-1} (5.11 μm), which is in quite good agreement with the expected value of (5.3 μm).[8]

The threshold current densities obtained in pulsed and cw mode at different temperatures are displayed in Fig. 3(b). Note that the measurements shown were taken without (pulsed mode) and with (cw) the HR coating on the backfacet of the laser. From an exponential fit of the data, the characteristic temperature T_0 can be deduced. It yields 207 and 111 K in pulsed and cw mode, respectively. The thermal resistance R_{th} of the device can be estimated at 243 K by comparing the threshold current density in cw obtained without HR coating (3.29 kA/cm^2) and the pulsed measurements displayed in Fig. 3(b). This leads to a value of R_{th} equal to 14.5 K/W corresponding to a thermal conductance G_{th} =516 W/K cm^{-2}. From the change of current density before and after the deposition of the HR coating, the waveguide losses can be estimated and yield 9.7 cm^{-1}. The performances reported in Figs. 3(a) and 3(b) are similar to those reported in Refs. 8 and 9 although a direct comparison is not as straight-forward as in the case of the bound-to-continuum samples. Slightly lower performance is however, anticipated for the MOVPE-grown lasers since the linewidth of the electroluminescence peak measured at room temperature is broader (36 meV) than the corresponding value (25 meV) found in Ref. 8 and 9.

In conclusion our results demonstrate the realization of strained QCLs based on a bound-to-continuum design which operate in pulsed mode above 320 K with a very low threshold current density. Devices based on a double phonon resonance design and processed into buried heterostructures lasers worked in continuous wave up to 280 K. The results presented in this letter are comparable with those of equivalent structures grown by molecular beam epitaxy. The performance level can be improved in many ways, including the optimization of the processing of buried heterostructure devices as well as the doping in the active region. It will allow without doubts the cw operation at 300 K of these lasers. Another remarkable finding is the low threshold current densities (less than 2 kA/cm^2) measured at room temperature with lasers deposited at a high growth rate of 0.5 nm/s. Altogether, the results presented in this letter demonstrate that MOVPE is a viable solution to grow high performance low-threshold strained QCLs operating in cw at room temperature.

The Harvard group acknowledges partial financial support from Agilent Technologies, from the U.S. Army Research Laboratory and the U.S. Army Research Office under Grant No. W911NF-04-1-0253. Part of the processing was done at the Center for Nanoscale Systems (CNS) at Harvard University. Harvard-CNS is a member of the National Nanotechnology Infrastructure Network (NNIN).

[1] A. Kosterev and F. Tittel, IEEE J. Quantum Electron. **38**, 582 (2002).
[2] J. Yu, S. Slivken, S. Darvish, A. Evans, B. Gokden, and M. Razeghi, Appl. Phys. Lett. **87**, 041104 (2005).
[3] S. Blaser, D. Yarekha, L. Hvozdara, Y. Bonetti, A. Muller, M. Giovannini, and J. Faist, Appl. Phys. Lett. **86**, 41109 (2005).
[4] R. P. Green, L. R. Wilson, E. A. Zibik, D. G. Revin, J. W. Cockburn, C. Pflügl, W. Schrenk, G. Strasser, A. B. Krysa, J. S. Roberts, C. M. Tey, and A. G. Cullis, Appl. Phys. Lett. **85**, 5529 (2004).
[5] D. Bour, M. Troccoli, F. Capasso, S. Corzine, A. Tandon, D. Mars, and G. Höfler, J. Cryst. Growth **272**, 526 (2004).
[6] M. Troccoli, D. Bour, S. Corzine, G. Höfler, A. Tandon, D. Mars, D. Smith, L. Diehl, and F. Capasso, Appl. Phys. Lett. **85**, 5842 (2004).
[7] J. Faist, F. Capasso, D. Sivco, A. Hutchinson, S. Chu, and A. Cho, Appl. Phys. Lett. **72**, 680 (1998).
[8] D. Hofstetter, M. Beck, T. Aellen, and J. Faist, Appl. Phys. Lett. **78**, 396 (2001).
[9] D. Yarekha, M. Beck, S. Blaser, T. Aellen, E. Gini, D. Hofstetter, and J. Faist, IEEE Electron Device Lett. **39**, 1123 (2003).

Downloaded 31 Jan 2006 to 128.103.60.225. Redistribution subject to AIP license or copyright, see http://apl.aip.org/apl/copyright.jsp

High-power quantum cascade lasers grown by low-pressure metal organic vapor-phase epitaxy operating in continuous wave above 400 K

L. Diehl
Division of Engineering and Applied Science, Cruft Laboratory 310, Harvard University, 19 Oxford Street, Cambridge, Massachusetts 02138

D. Bour, S. Corzine, J. Zhu, and G. Höfler
Agilent Laboratories, 3500 Deer Creek Road, Palo Alto, California 94304

M. Lončar, M. Troccoli, and Federico Capasso[a)]
Division of Engineering and Applied Science, Cruft Laboratory 310, Harvard University, 19 Oxford Street, Cambridge, Massachusetts 02138

(Received 28 December 2005; accepted 14 April 2006; published online 17 May 2006)

High-power quantum cascade lasers (QCLs) working in continuous wave (cw) above 400 K are presented. The material was grown by low-pressure metal organic vapor-phase epitaxy and processed into narrow buried heterostructure lasers. A cw output power of 204 mW was obtained at 300 K with an 8.38 μm wavelength, 3 mm long and 7.5 μm wide coated laser. The device operates in cw mode above 400 K, which exceeds the previous maximum cw temperature operation of QCLs by approximately 60 K. Preliminary reliability data obtained by accelerated aging tests indicate a remarkable robustness of the lasers. © *2006 American Institute of Physics*.
[DOI: 10.1063/1.2203964]

It has been shown in the last few years that quantum cascade lasers (QCLs) are an ideal light source for many chemical sensing applications in the midinfrared.[1,2] Indeed stable single mode operation, which is highly desirable for these applications can be achieved with QCLs by means of an external cavity[3] or by fabricating distributed feedback lasers,[4] for example. In addition, QCLs can work in continuous wave (cw) at temperatures above 300 K with high output power, as discussed in Refs. 4 and 5. A recent article reported a cw power of 446 mW at 292 K and a maximum temperature operation of 333 K for a 15 μm wide, 3 mm long device emitting at 6 μm.[6] As the commercial significance of QCLs increases, the production of reliable and potentially low-cost devices becomes increasingly important. The question of whether or not high performance can be obtained from QCLs grown by metal organic vapor-phase epitaxy (MOVPE) is central since this technique is a widely established platform for the high-volume production of reliable semiconductor lasers. This question was partially answered recently by the demonstration of room temperature cw operation with lattice matched QCLs grown by MOVPE.[7] The devices tested, which were based on a basic three quantum well active region design, worked cw up to 320 K with an output power of more than 20 mW at 300 K.

In this letter we report the fabrication of MOVPE-grown QCLs having performance comparable to the best results obtained with MBE material.[6] The maximum collected output power from a 7.5 μm wide, 3 mm long QCL is as high as 204 mW at 300 K after the evaporation of a high-reflection (HR) coating. This device operated in continuous mode up to 400 K with more than 10 mW of output power. Note that throughout this letter, the values of the output power and the slope efficiency are not corrected for the collection efficiency of our setup, which is estimated to be 70%.

The QCLs investigated here were grown by low-pressure MOVPE in a standard reactor equipped with a purged and pressure-balanced switching manifold and a close-spaced showerhead injector. More details about the growth can be found in Refs. 8 and 9. The active region of the samples studied is based on a double-phonon resonance design identical, except for the doping level in the injector, to the design reported by Hofstetter *et al.*[10] 35 states were grown at a slow rate of 0.1 nm/s. The doping in the injector was kept low (1×10^{17} cm^3) to limit the optical losses. The waveguide surrounding the active region consists of two InGaAs layers (thickness of 0.52 μm, Si:doping of 3×10^{16} cm^3) and two thick InP cladding layers (thickness of 3.5 μm, Si:doping of 1×10^{17} cm^3) grown at a fast rate of 0.5 nm/s. The growth sequence ended with the deposition of a plasmon-confinement layer (InP, thickness of 0.5 μm, Si:doping of 5×10^{18} cm^3) and 20 nm n^+ InGaAs capping layer.

Buried heterostructure lasers were processed using conventional fabrication techniques. Ridges with a width of either 3 or 7.5 μm were etched by a combination of wet and dry etching. Fe-doped InP was then regrown to planarize the structure, helping to decouple laterally the optical mode from the lossy metal contacts and to lower the thermal resistance of the device while minimizing leakage currents. Electrical contacts are provided by Ti/Au metallizations evaporated directly onto the n^+ InGaAs capping layer and the Fe:InP surrounding the laser ridge. An additional 5 μm thick gold layer was subsequently electroplated to further improve heat dissipation. The devices were finally mounted ridge side up onto copper blocks and wire bonded. The lasers were tested inside a Peltier-cooled box with a CaF_2 window. The temperature of the heat sink was monitored with a Si diode placed near the QCLs. The light from one facet was collected by $f/1$ optics and a calibrated thermopile detector was used to perform power measurements. The optical spectra were recorded with a Nicolet 860 Fourier transform interferometer.

Figure 1 shows the voltage and the light intensity versus current (*V-I* and *L-I*) curves of 3 mm long lasers having,

[a)]Electronic mail: capasso@deas.harvard.edu

 © 2006 American Institute of Physics
Downloaded 25 May 2006 to 128.103.60.225. Redistribution subject to AIP license or copyright, see http://apl.aip.org/apl/copyright.jsp

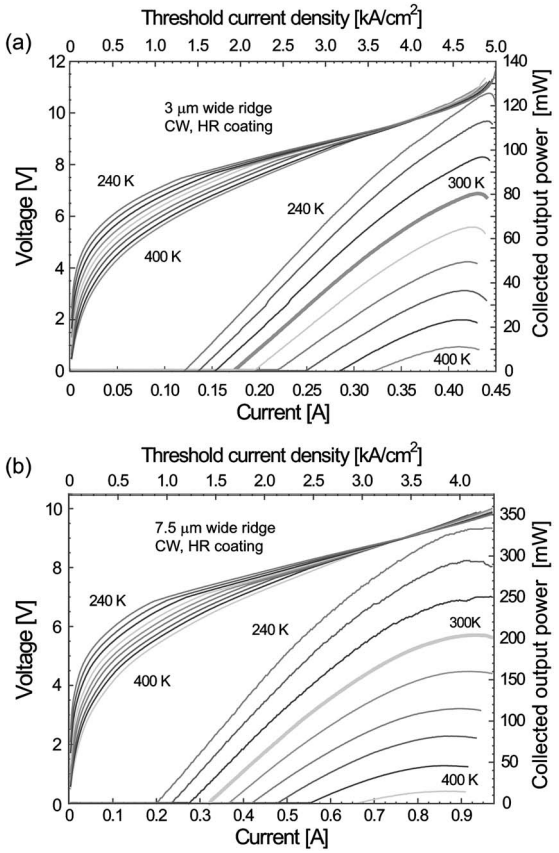

FIG. 1. cw *L-I* and *V-I* curves of HR coated 3 mm long lasers with (a) 3 μm and (b) 7.5 μm ridge widths. The heat sink temperature was varied between 240 and 400 K in steps of 20 K. The optical power data, taken from one laser facet, are not corrected for the estimated 70% collection efficiency of our setup.

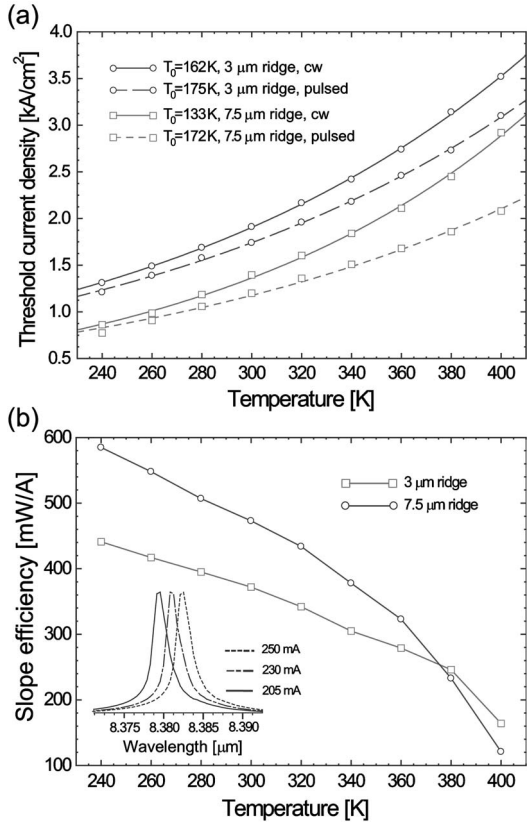

FIG. 2. (a) Threshold current density as a function of heat sink temperature for the HR coated, 3 mm long lasers with 3 μm (circles) and 7.5 μm (squares) ridge width in pulsed (dashed line) and cw modes (solid line). The experimental points (open symbols) are fitted by the expression $j_{\mathrm{th}}=j_0\, e^{T/T_0}$. (b) Slope efficiency vs temperature deduced from the *L-I* curves shown in Fig. 1(b) close to threshold. Inset: high-resolution cw spectra as a function of injection current measured with the 3 μm wide QCL without HR coating at a constant temperature of 300 K.

respectively, 3 and 7.5 μm ridge widths. The measurements were performed with the devices operating in cw mode and at temperatures ranging from 240 to 400 K. A HR coating consisting of 200 nm Al_2O_3 and 30 nm Au was evaporated on the backfacet of both devices and nearly doubled the maximum collected output power P_{max} of both the narrow and the broad laser. The value of P_{max}, measured at room temperature with the 7.5 μm wide QCL, was indeed 115 and 204 mW before and after the deposition of the HR coating. Note that the total output power after backfacet coating should be as high as 291 mW given the estimated collection efficiency. The above improvement was accompanied by a decrease of approximately 20% of the threshold current density of both devices. From this change, an estimate of the waveguide losses was deduced and yields 8.3 and 9 cm^{-1} for the broad and the narrow laser, respectively.

A remarkable feature is that both lasers work in continuous mode at 400 K with more than 10 mW of output power. It exceeds the previous maximum cw temperature operation of QCLs by approximately 60 K.[11] At room temperature, the maximum collected output power reaches 80 and 204 mW with a corresponding slope efficiency dP/dI equal to 372 and 473 mW/A for the narrow and the broad laser, respectively. In a QCL, as the current is increased above threshold, an electron creates a number of photons equal to the number of stages N. It is thus appropriate to define a differential quantum efficiency *per stage* as $\eta_d = e\,(Nh\nu)^{-1}\, dP/dI$ with $h\nu$ the photon energy. Note that P in this equation is equal to the power collected from a single facet of a HR coated laser. If the 70% collection efficiency of our setup is taken into account, η_d yields, in the case of the HR coated 7.5 μm wide QCL, 13.1% and 3.32% at, respectively, 300 and 400 K. With these numbers and the estimate of the internal loss $\alpha_{\mathrm{waveguide}}$, the internal quantum efficiency (per stage) η_i can be found from the standard formula $\eta_i = \eta_d(1 + \alpha_{\mathrm{waveguide}}/\alpha_{\mathrm{mirror}})$, where $\alpha_{\mathrm{mirror}} = 2.15\ \mathrm{cm}^{-1}$ is the mirror loss. When $\eta_d = 13.1\%$, the internal quantum efficiency is about 63.7%, which is comparable to standard edge-emitting diode lasers.

The value of the threshold current density j_{th} measured in cw and pulsed mode (1.5% duty cycle, 80 KHz repetition rate) is plotted as a function of temperature in Fig. 2(a). The pulsed threshold current of the narrow device is approximately 44% larger than the value found for the broad laser. This percentage difference is essentially constant over the entire temperature range and is explained by the reduction of the overlap of the optical mode with the gain medium as the stripe width narrows. j_{th} is indeed proportional to the total optical losses divided by the overlap factor Γ. Using the waveguide loss mentioned earlier in the text and the values of Γ calculated with a two-dimensional (2D) beam-propagation modeling program (38% and 55% for the narrow and the broad QCL, respectively), j_{th} is found to be 54% larger for the 3 μm wide lasers compared to the broad device, in good agreement with the experimental data. The cw threshold current densities of the 3 μm wide laser are 1.9 $\mathrm{kA/cm}^2$ at room temperature and 3.5 $\mathrm{kA/cm}^2$ at 400 K.

Downloaded 25 May 2006 to 128.103.60.225. Redistribution subject to AIP license or copyright, see http://apl.aip.org/apl/copyright.jsp

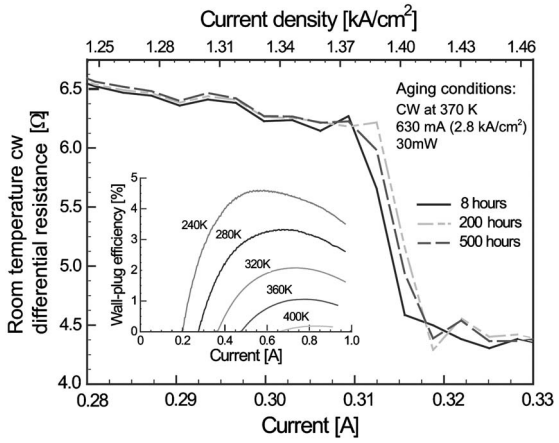

FIG. 3. Room temperature cw differential resistance of the 7.5 μm HR coated device as a function of current after 8, 200, and 500 h of cw operation at 370 K. The discontinuity indicates the position of the threshold current. Inset: wall-plug efficiency as a function of current for temperatures ranging from 240 to 400 K.

As in pulsed mode, the corresponding values for the wider laser are lower (1.39 kA/cm^2 at 300 K and still less than 3 kA/cm^2 at 400 K).

It is apparent from Figs. 1 and 2(a) that the 7.5 μm wide ridge is the most sensitive of the two samples with respect to temperature changes. The characteristic temperature T_0, which describes phenomenologically the increase of j_{th} with temperature, has a similar value in pulsed mode for both the narrow and the broad laser. A much larger T_0 is found, however, in continuous mode for the 3 μm wide device, which confirms that a narrow stripe width leads to performance less sensitive to temperature. This conclusion is supported by Fig. 2(b), in which the slope efficiency is plotted as a function of temperature. The value of dP/dI clearly decreases faster for the device with a broader ridge as the temperature increases and above 380 K, the slope efficiency of the narrowest sample even becomes larger. The better heat removal capability of the narrow stripe laser translates into a higher value of the thermal conductance $G_{th}=(R_{th}A)^{-1}$. Here A is the device area and R_{th} (10.84 and 11.79 K/W for the 3 and 7.5 μm device at 300 K) is the thermal resistance which can be determined from the threshold current density versus temperature curves shown in Fig. 2(b).[6] At 300 K, the thermal conductance yields 942 and 394 W/Kcm^2 for, respectively, the narrow and the broad device. Note that the G_{th} ratio of 2.39 is very close to the stripe width ratio of 2.5. The larger value of G_{th} found for the 3 μm stripe is understandable as the ratio of volume to area is more favorable in terms of heat dissipation for narrower ridges. Similar conclusions were reached in previous studies.[12]

The inset of Fig. 2(b) shows typical emission spectra obtained above threshold with the devices investigated in the present letter. The different curves were measured at 300 K with a 3 μm wide laser operating in continuous mode. The emission wavelength is 8.38 μm and little shorter than the one of Refs. 10. Note that the optical spectra broadened and showed lasing in many modes when the devices were pumped at current densities at least 30% above j_{th}. A detailed study of this phenomenon will be published elsewhere. The wall-plug efficiency, defined as the total optical output power divided by the electrical input power, is shown in the inset of Fig. 3 for the HR coated 7.5 μm wide device. The *I-V* and *L-I* curves presented in Fig. 1(b) were used in the calculations. The wall-plug efficiency is as high as 4.6% at 240 K and 0.18% at 400 K. Given the estimated collection efficiency of our setup, these values should be approximately a factor of 1/0.7 larger.

Preliminary results obtained in the context of accelerated aging measurements are also promising. The 7.5 μm wide laser, whose performance is described in this letter was operated for long periods of time in cw at 370 K and a constant current of 630 mA, corresponding to an output power of 30 mW and a current density of 2.8 kA/cm^2. At regular intervals, the cw *L-I* and *I-V* curves were measured at 300 K. After more than 500 h, only negligible variations in the threshold current and slope efficiency were observed. Figure 3 shows, for example, the differential resistance of the device, deduced from the *I-V* curves measured at room temperature after 8, 200, and 500 h of cw operation at 370 K. The threshold current corresponds to the discontinuity in each of the traces. It varies between curves by less than 2 mA. This change (approximately 0.6%) is insignificant as it is comparable to the measurement error. The latter is equal to 3 mA and is due to the fact that the heat sink temperature is only controlled within 0.2 K. Note that the box in which the laser was mounted was not purged with dry air or nitrogen. A more detailed description of the results will be given elsewhere.

In conclusion, 8.38 μm wavelength, HR coated QC lasers grown by low-pressure MOVPE and processed into narrow buried heterostructures were operated in cw mode up to 400 K. High cw output powers as high as 204 mW at room temperature and more than 10 mW at 400 K were measured. The laser characteristics reported here represent a significant improvement in the performance of MOVPE-grown QCLs.

The Harvard group acknowledges partial financial support from Agilent Technologies, from the U.S. Army Research Laboratory and the U.S. Army Research Office under Grant No. W911NF-04-1-0253 and from DARPA (optofluidic center) under Grant No. HR0011-04-1-0032. Support from the Center for Nanoscale Systems (CNS) at Harvard University is also gratefully aknowledged. Harvard-CNS is a member of the National Nanotechnology Infrastructure Network (NNIN).

[1] A. A. Kosterev and F. K. Tittel, IEEE J. Quantum Electron. **38**, 582 (2002).
[2] D. D. Nelson, J. H. Shorter, J. B. McManus, and M. S. Zahniser, Appl. Phys. B: Lasers Opt. **75**, 343 (2002).
[3] R. Maulini, S. Yarekha, J. M. Bulliard, M. Giovannini, and J. Faist, Opt. Lett. **30**, 2584 (2005).
[4] J. S. Yu, S. Slivken, S. R. Darvish, A. Evans, G. Gokden, and M. Razeghi, Appl. Phys. Lett. **87**, 041104 (2005).
[5] A. Evans, J. S. Yu, S. Slivken, and M. Razeghi, Appl. Phys. Lett. **85**, 2166 (2004).
[6] A. Evans, J. S. Yu, J. David, L. Doris, K. Mi, S. Slivken, and M. Razeghi, Appl. Phys. Lett. **84**, 314 (2004).
[7] M. Troccoli, S. Corzine, D. Bour, J. Zhu, O. Assayag, L. Diehl, B. G. Lee, G. Höfler, and F. Capasso, Electron. Lett. **41**, 1059 (2005).
[8] D. Bour, M. Troccoli, F. Capasso, S. Corzine, A. Tandon, D. Mars, and G. Höfler, J. Cryst. Growth **272**, 526 (2004).
[9] M. Troccoli, D. Bour, S. Corzine, G. Höfler, A. Tandon, D. Mars, D. J. Smith, L. Diehl, and F. Capasso, Appl. Phys. Lett. **85**, 5842 (2004).
[10] D. Hofstetter, M. Beck, T. Aellen, J. Faist, U. Oesterle, M. Ilegems, E. Gini, and H. Melchior, Appl. Phys. Lett. **78**, 1964 (2001).
[11] W. W. Bewley, J. R. Lindle, C. Soo Kim, I. Vurgaftman, J. R. Meyer, A. J. Evans, J. Su Yu, S. Slivken, and M. Razeghi, IEEE J. Quantum Electron. **41**, 833 (2005).
[12] S. Slivken, J. S. Yu, A. Evans, J. David, L. Doris, and M. Razeghi, IEEE Photon. Technol. Lett. **16**, 744 (2004).

Downloaded 25 May 2006 to 128.103.60.225. Redistribution subject to AIP license or copyright, see http://apl.aip.org/apl/copyright.jsp

High-temperature continuous wave operation of strain-balanced quantum cascade lasers grown by metal organic vapor-phase epitaxy

L. Diehl[a)]
Division of Engineering and Applied Sciences, Harvard University, Cambridge, Massachusetts 02138

D. Bour, S. Corzine, J. Zhu, and G. Höfler
Agilent Laboratories, 3500 Deer Creek Road, Palo Alto, California 94304

M. Lončar, M. Troccoli, and Federico Capasso[b)]
Division of Engineering and Applied Sciences, Harvard University, Cambridge, Massachusetts 02138

(Received 18 April 2006; accepted 28 June 2006; published online 21 August 2006)

The authors report the fabrication of high-power strained quantum cascade lasers working in continuous mode above 370 K. The devices, processed in narrow buried heterostructures, were grown by low-pressure metal organic vapor-phase epitaxy. Continuous wave output power as high as 312 mW at 300 K was obtained at a wavelength of 5.29 μm from a 3.25 mm long, 7.5 μm wide laser with a high-reflectivity back facet coating. The slope efficiency was in excess of 1.5 W/A and the power conversion efficiency reached almost 5%. © *2006 American Institute of Physics*.
[DOI: 10.1063/1.2337284]

In the past few years, the performance of quantum cascade lasers[1] (QCLs) grown by molecular beam epitaxy (MBE) has improved tremendously and high-power continuous wave (cw) operation at room temperature has been since routinely achieved at various wavelengths.[2,3] Short-wavelength (5.25 μm) QCLs with a maximum cw output power of 480 mW were reported in Ref. 4. This result was obtained at room temperature (298 K) with a strained QC structure based on a double-phonon resonance[1] processed into 11 μm wide ridge waveguide. Together with the large cw output power achievable by QCLs at room temperature, the wavelength range accessible to these devices makes them very attractive, in particular, for compact gas sensors based on photoacoustic spectroscopy.[5]

Metal organic vapor-phase epitaxy (MOVPE) is a widely established platform for the high-volume production of low cost and reliable semiconductor lasers. This technique allows the deposition of uniform and thick layers at high rates. It offers also excellent stability over long growth runs and short machine downtime. MOVPE is thus particularly well suited for the industrial production of QCLs. Recent work showed that the performance obtained with lattice-matched and strained QCLs deposited by MOVPE is comparable with that of similar structures grown by MBE.[6–8] Recently, we demonstrated high-power ($\cong$200 mW) cw operation at room temperature of $\lambda \cong 8.38$ μm lattice-matched QCLs grown by MOVPE.[9]

In the present letter, we report the cw operation of strained QCLs at temperatures ranging from 300 to 385 K. The devices studied were processed into buried heterostructures and a high-reflectivity (HR) coating was evaporated on the back facet. With a 7.5 μm wide 3.25 mm long back facet coated laser, we measured low threshold current densities at room temperature equal to 1.23 kA/cm^2 in pulsed mode and to 1.53 kA/cm^2 in cw, together with high cw output power in excess of 300 mW at 300 K. The maximum operating temperature was as high as 376 K for this particular device. This represents a major improvement compared to our previous results obtained with similar devices, which operated only up to approximately 280 K in cw mode.[8]

The QCL structure studied in the present work was deposited on a heavily doped n-type ($n \approx 3 \times 10^{18}$ cm^3) InP substrate by low-pressure (76 Torr) MOVPE without growth interruption at the barrier/quantum well interfaces. The growth conditions were similar to the ones described in Refs. 7–9. The deposition rate was 0.5 nm/s throughout the structure, except for the active region, which was grown at a slower rate of 0.1 nm/s. The cladding layers consist of a 3.5 μm thick InP layer doped with silicon ($n \approx 1 \times 10^{17}$ cm^3). The lower cladding layer helps in decoupling the optical mode from the heavily doped substrate, preventing substantial free-carrier absorption. The waveguide core is composed of two 0.33 μm thick n-doped ($n \approx 3 \times 10^{16}$ cm^3) InGaAs layers and the active region. The latter comprises 30 stages and is based on a double-phonon resonance design identical, except for the doping level in the injector, to the one reported by Hofstetter *et al.*[10] The growth ended with a 0.5 μm thick InP plasmon-enhanced confinement[1] layer doped with silicon ($n \approx 5 \times 10^{18}$ cm^3), followed by two heavily doped contact layers (10 nm, $n+$ InP/20 nm, $n+$ InGaAs). Overall, the structure described above is very similar to the double-phonon laser reported in a previous article.[8] The main difference resides in the doping level being lowered by a factor of 2 in all of the doped layers comprising the claddings and waveguide core (including the active region).

The grown structure was processed into buried heterostructure lasers. Ridges 3 and 7.5 μm wide were defined by conventional photolithography techniques and etched down to approximately half of the lower cladding layer by reactive ion etching. Using MOVPE, InP doped with Fe was then selectively regrown around the ridges to enhance the lateral heat dissipation from the active region. The level of Fe doping was chosen to slightly exceed the background doping of the MOVPE reactor. Since Fe atoms introduced in InP act as

[a)]Electronic mail: ldiehl@deas.harvard.edu
[b)]Electronic mail: capasso@deas.harvard.edu

 © 2006 American Institute of Physics
Downloaded 25 Aug 2006 to 128.103.60.225. Redistribution subject to AIP license or copyright, see http://apl.aip.org/apl/copyright.jsp

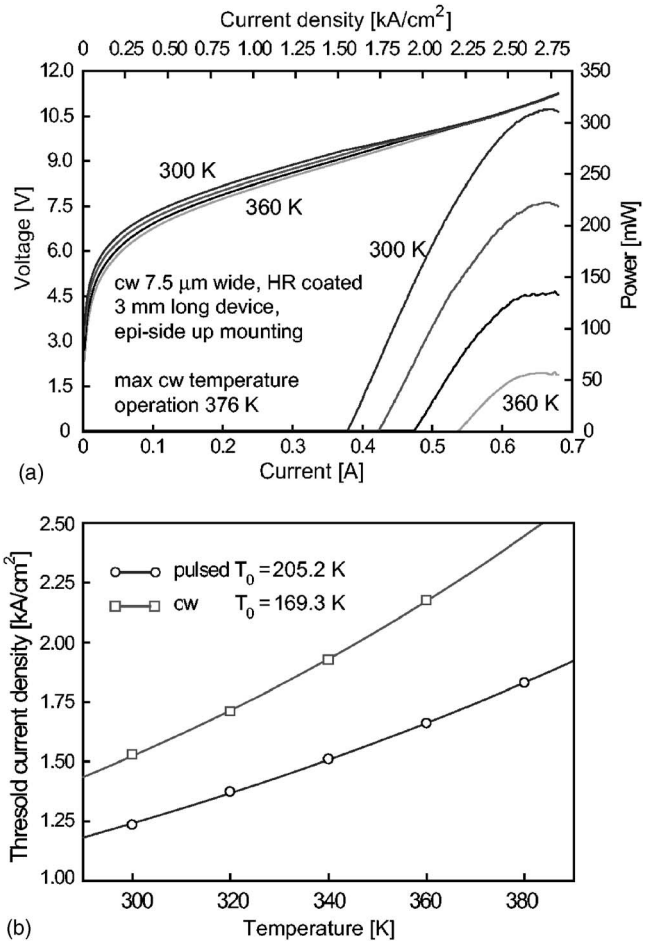

FIG. 1. (a) *V-I/L-I* curves obtained at different temperatures in cw mode with a 7.5 μm wide, 3.25 mm long HR-coated device. (b) Threshold current density measured in pulsed and cw modes vs temperature. The experimental points were fitted with the empirical relation $j_{th}=j_0\exp(T/T_0)$.

deep carrier traps, there are essentially no free electrons in the regrown InP layer, resulting in insulating and optically transparent regions around the laser ridges. The next fabrication steps include the evaporation of Ti/Au top contacts followed by the electroplating of a 5 μm thick Au layer. Thinning of the substrate and the deposition of a Ge/Au back contact finished the processing. The devices were subsequently cleaved into cavities of different lengths before being soldered episide up onto Cu heat sinks. A HR coating consisting of Al_2O_3/Au (200/30 nm) layers was evaporated on the back facet of the QCLs. The voltage and output power versus current (*V-I/L-I*) characteristics were obtained with the devices placed into a box equipped with thermoelectric cooler. The output power was measured using a polished metallic pipe guiding the light from the laser front facet directly onto the surface of a calibrated thermopile detector. The collection efficiency of this setup is considered to be near 100%. The spectral characterization was performed with a Fourier transform infrared spectrometer equipped with a deuterated triglycine sulphate detector.

The *V-I/L-I* curves obtained in continuous mode from a 3.25 mm long, 7.5 μm wide and HR-coated QCLs are shown in Fig. 1(a). The cw threshold current density j_{th} for this device was 1.53 kA/cm^2 at room temperature and the corresponding slope efficiency was 1.570 W/A. The largest output powers obtained at 300 and 360 K were 312 and 57 mW, respectively. The highest cw temperature operation T_{max} was 376 K and by reducing the temperature to 260 K, more than 500 mW of cw output power was achieved. The maximum wall-plug efficiency, defined as the total optical power divided by the electrical power, reached 4.6% at 300 K. This device has performance comparable to the best and most recent results obtained with slightly broader MBE-grown QCLs emitting at the same wavelength.[4]

Figure 1(b) is a plot of the threshold current densities obtained at various heat sink temperatures from the HR-coated device described in the previous paragraph. These data were deduced from the cw measurements presented in Fig. 1(a) and from measurements obtained in pulsed mode. In the latter case, the repetition rate was 80 kHz and the pulse width was 125 ns. From these data, high characteristic temperatures T_0 equal to 205.2 K in pulsed mode and 169.3 K in cw mode were deduced. T_0 describes empirically the increase in threshold current versus temperature according to an exponential function $j_{th}(T)=j_0\exp(T/T_0)$. The thermal resistance of the device R_{th} can also be calculated from the measurements presented in Fig. 1(b) and yields 12.14 K/W at 300 K.[11] It corresponds to a thermal conductance $G_{th}=1/(AR_{th})=337.9$ W/(K cm^2), where A is the device area. Using the value found for R_{th}, the temperature difference ΔT between the heat sink and the active region reaches at 300 K $\Delta T=R_{th}P_{elec}=42.8$ K. Here P_{elec} is the electrical power dissipated in the device.

Figures 2(a) and 2(b) show data qualitatively similar to those displayed in Fig. 1. This second set of measurements was, however, obtained from a 3 μm wide laser. The other device characteristics such as the cavity length were otherwise identical. The cw output power was as high as 97 mW at 300 K, which is noteworthy given the narrow width of this QCL. The corresponding slope efficiency was 1.19 W/A. The threshold current densities measured at room temperature were 1.39 and 1.43 kA/cm^2 in pulsed and cw modes, respectively. The value of j_{th} in pulsed mode is only slightly larger than the one obtained with the 7.5 μm wide structure. This is consistent with the results of two-dimensional mode profile simulations, which showed that the mode overlap factor Γ is comparable for both the narrow and broad samples (53.3% and 61.6%, respectively). The inset of Fig. 3 shows a typical spectrum obtained at a current 5% above threshold with the narrow QCL. Note that when the devices studied are pumped 30% or more above j_{th}, the optical spectrum broadens and is composed by many neighboring longitudinal modes. A detailed study of this phenomenon will be given elsewhere. The emission wavelength is 5.29 μm and is very close to the designed value.[10]

The thermal resistance for the narrowest QCL is 7.01 K/W, which translates into $G_{th}=1461$ W/K cm^2. This value is comparable to the one found for state-of-the-art buried heterostructure QCLs whose performance was reported in Ref. 12. The ratio of the thermal conductance found for the broad and narrow samples does not match the ratio of the lasers widths. However, it indicates clearly that lateral heat transfer is a major factor in the thermal resistance of the device. This is also in agreement with the fact that the quantity T_0 has a comparable value in pulsed and cw modes for the narrow device (pulsed mode, $T_0=189.3$ K; cw mode, $T_0=185.7$ K), while T_0 in the case of the 7.5 μm QCL decreases by almost 35 K (pulsed mode, $T_0=205.2$ K; cw mode, $T_0=169.3$ K).

Downloaded 25 Aug 2006 to 128.103.60.225. Redistribution subject to AIP license or copyright, see http://apl.aip.org/apl/copyright.jsp

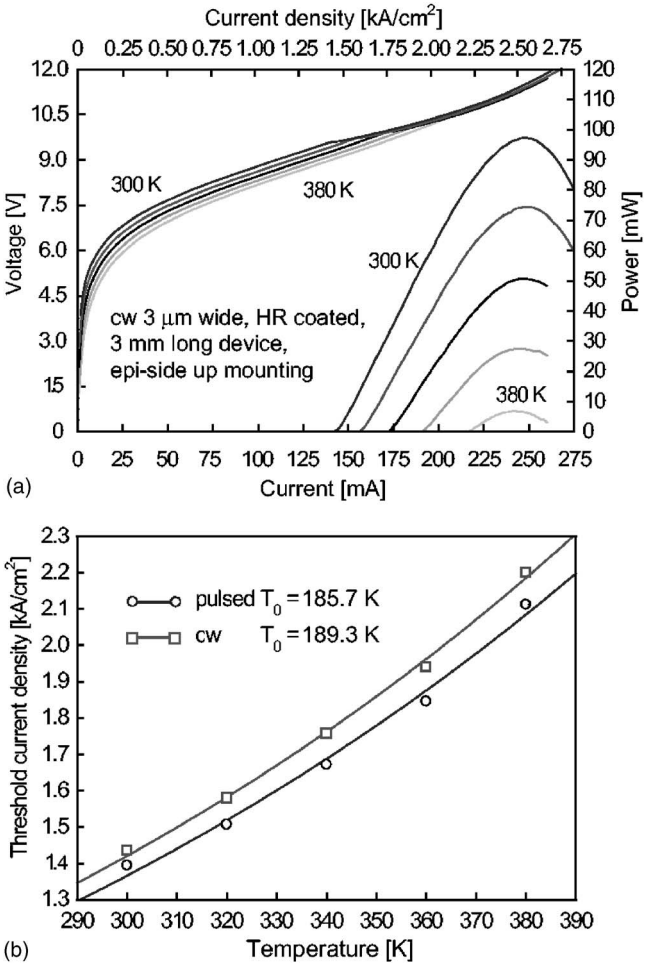

FIG. 2. (a) *V-I*/*L-I* curves obtained at different temperatures in cw mode with a 3 μm wide, 3.25 mm long HR-coated device. (b) Threshold current density measured in pulsed and cw modes vs temperature. The experimental points were fitted with the empirical relation $j_{th}=j_0\exp(T/T_0)$.

Three μm wide, HR-coated devices with different cavity lengths were also measured. The longest sample (4.25 mm) had the highest cw operating temperature (385 K) and the largest output power, which reached 136 mW at 300 K. The threshold current density measured in pulsed mode for 1.09, 1.75, 2.25, 3.25, and 4.25 mm long cavity is reported in Fig. 3 as a function of the inverse of the cavity length. From these data, the waveguide losses α_w were deduced assuming that the gain cross section does not depend on the current density.[13] The value of α_w calculated from the fit of the experimental points is only 3.8 cm^{-1}, which compares well with the numbers reported in Ref.[14]

In summary, we have presented the high-power cw operation at high temperature of 5.29 μm wavelength strained QCLs grown by low-pressure MOVPE. The characteristics of our lasers are comparable to the best and most recent results obtained from MBE-grown material. Our devices have the highest operating cw temperature reported so far for QCLs at this wavelength. The present work demonstrates that MOVPE meets all the requirements necessary to grow high-performance state-of-the-art QCLs, even with demanding material constraints such as large strain.

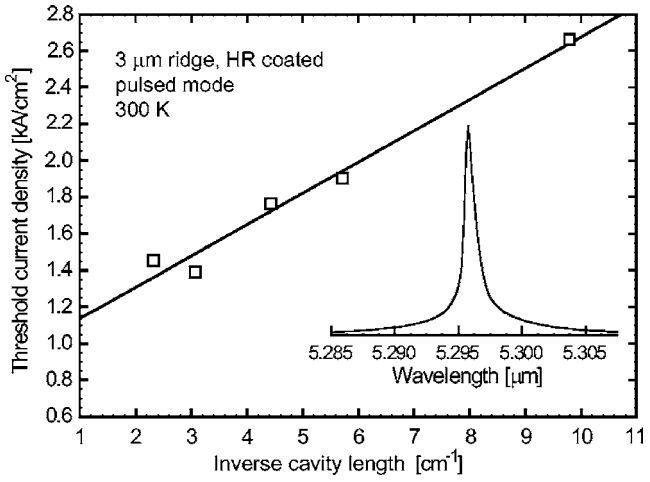

FIG. 3. Pulsed threshold current density and device thermal resistance measured at 300 K with 3 μm wide HR-coated lasers having a different cavity length. The inset shows an optical spectrum measured with the 3 μm wide, 3.25 mm long HR-coated device operated in cw mode close to threshold.

The Harvard group acknowledges partial financial support from Agilent Technologies, from the U.S. Army Research Laboratory and the U.S. Army Research Office under Grant No. W911NF-04-1-0253, and from DARPA (Optofluidics Center) under Grant No. HR0011-04-1-0032. The Center for Nanoscale Systems (CNS) at Harvard University is also gratefully acknowledged. Harvard-CNS is a member of the National Nanotechnology Infrastructure Network (NNIN).

[1] F. Capasso, C. Gmachl, D. L. Sivco, and A. Y. Cho, Phys. Today **55**(5), 34 (2002).
[2] J. S. Yu, S. Slivken, A. Evans, S. R. Darvish, J. Nguyen, and M. Razeghi, Appl. Phys. Lett. **88**, 091113 (2006).
[3] J. S. Yu, S. Slivken, A. Evans, S. R. Darvish, J. Nguyen, and M. Razeghi, Appl. Phys. Lett. **88**, 091113 (2006).
[4] A. Evans, J. Nguyen, S. Slivken, J. S. Yu, S. R. Darvish, and M. Razeghi, Appl. Phys. Lett. **88**, 51105 (2006).
[5] A. Kosterev and F. Tittel, IEEE J. Quantum Electron. **38**, 582 (2002).
[6] R. P. Green, L. R. Wilson, E. A. Zibik, D. G. Revin, J. W. Cockburn, C. Pflügl, W. Schrenk, G. Strasser, A. B. Krysa, J. S. Roberts, C. M. Tey, and A. G. Cullis, Appl. Phys. Lett. **85**, 5529 (2004).
[7] M. Troccoli, S. Corzine, D. Bour, J. Zhu, O. Assayag, L. Diehl, B. G. Lee, G. Höfler, and F. Capasso, Electron. Lett. **41**, 1059 (2005).
[8] L. Diehl, D. Bour, S. Corzine, J. Zhu, G. Höfler, B. G. Lee, C. Y. Wang, M. Troccoli, and F. Capasso, Appl. Phys. Lett. **88**, 041102 (2006).
[9] L. Diehl, D. Bour, S. Corzine, J. Zhu, G. Höfler, M. Lončar, M. Troccoli, and F. Capasso, Appl. Phys. Lett. **88**, 201115 (2006).
[10] D. Hofstetter, M. Beck, T. Aellen, and J. Faist, Appl. Phys. Lett. **78**, 396 (2001).
[11] S. Blaser, D. A. Yarekha, L. Hvozdara, Y. Bonetti, A. Müller, M. Giovannini, and J. Faist, Appl. Phys. Lett. **86**, 41109 (2005).
[12] A. Evans, J. S. Yu, J. David, L. Doris, K. Mi, S. Slivken, and M. Razeghi, Appl. Phys. Lett. **84**, 314 (2004).
[13] C. Sirtori, J. Faist, F. Capasso, D. Sivco, A. Hutchinson, and A. Cho, Appl. Phys. Lett. **66**, 3242 (1995).
[14] T. Gresch, M. Giovannini, N. Hoyler, and J. Faist, IEEE Photon. Technol. Lett. **18**, 544 (2006).

Downloaded 25 Aug 2006 to 128.103.60.225. Redistribution subject to AIP license or copyright, see http://apl.aip.org/apl/copyright.jsp

PHYSICAL REVIEW A **75**, 031802(R) (2007)

Coherent instabilities in a semiconductor laser with fast gain recovery

Christine Y. Wang,[1] L. Diehl,[2] A. Gordon,[3] C. Jirauschek,[3] F. X. Kärtner,[3,*] A. Belyanin,[4] D. Bour,[5] S. Corzine,[5] G. Höfler,[5] M. Troccoli,[2] J. Faist,[6] and Federico Capasso[2,†]

[1]*Department of Physics, Harvard University, Cambridge, Massachusetts 02138, USA*

[2]*School of Engineering and Applied Science, Harvard University, Cambridge, Massachusetts 02138, USA*

[3]*Department of Electrical Engineering and Computer Science and Research Laboratory of Electronics, Massachusetts Institute of Technology, 77 Massachusetts Avenue, Cambridge, Massachusetts 02139, USA*

[4]*Department of Physics, Texas A & M University, College Station, Texas 77843, USA*

[5]*Agilent Technologies, Palo Alto, California 94306, USA*

[6]*Institute of Physics, University of Neuchâtel, CH-2000 Neuchâtel, Switzerland*

(Received 11 July 2006; published 30 March 2007)

We report the observation of a coherent multimode instability in quantum cascade lasers (QCLs), which is driven by the same fundamental mechanism of Rabi oscillations as the elusive Risken-Nummedal-Graham-Haken (RNGH) instability predicted 40 years ago for ring lasers. The threshold of the observed instability is significantly lower than in the original RNGH instability, which we attribute to saturable-absorption nonlinearity in the laser. Coherent effects, which cannot be reproduced by standard laser rate equations, can play therefore a key role in the multimode dynamics of QCLs, and in lasers with fast gain recovery in general.

DOI: 10.1103/PhysRevA.75.031802 PACS number(s): 42.55.Px, 42.60.Mi, 42.65.Sf

The fundamental coherent mechanism that can destabilize a single-mode laser was predicted in the early 1960s [1] and was later extended to multimode lasers [2,3] where it became known as the Risken-Nummedal-Graham-Haken (RNGH) instability. These instabilities became classic landmarks for the general field of nonlinear dynamics [4,5] because they emerge in conceptually the simplest laser model, which in the single-mode case was shown to be equivalent to the Lorentz model of deterministic chaos [6]. Another feature that makes these instabilities so interesting and unique is their coherent nature that involves the polarization of the medium as a nontrivial dynamical variable. Most other physical mechanisms that can drive a laser from a single-mode to a multimode regime, such as spatial and spectral hole burning, Q switching, and saturable absorption [7,8], can be adequately described within the standard rate equation formalism, in which the polarization of the active medium is adiabatically eliminated. Both the single mode [1] and the multimode [2,3] instabilities cannot be explained by the rate equations. Such coherent effects can be only observed when the polarization is driven faster than or on a time scale comparable to the dephasing time T_2 [9].

The origin of the two coherent phenomena mentioned above is the oscillation of the population inversion at the Rabi frequency Ω_{Rabi} that takes place when the intracavity laser intensity becomes large. This results in a modification of the gain spectrum and the emergence of sidebands separated from the maximum of the gain curve by an amount corresponding to the Rabi frequency. These sidebands can be regarded as a manifestation of parametric gain. The instability sets in when the intracavity power is sufficiently large: the Rabi angular frequency Ω_{Rabi} has to be greater than the relaxation time scales of the gain medium [more precisely, Ω_{Rabi} is sufficiently greater than $(T_1T_2)^{-1/2}$, where T_1 is the gain relaxation time]. The instability threshold is often called the second laser threshold due to its universal nature.

Pioneering theoretical works stimulated extensive experimental studies that finally resulted in the observation of the Lorenz-type chaos in a far-infrared single-mode laser [10]. However, despite almost 40 years of efforts, the experimental demonstration of the multimode RNGH instability has remained somewhat controversial [11–16].

In lasers with long gain recovery compared to the cavity round-trip time, the instability caused by a saturable absorber can often lead to mode locking [8]. When the gain recovery time is short compared with the cavity round-trip time, it is usually assumed that the laser dynamics becomes very primitive and uninteresting (so-called class A laser). In this case mode locking is impossible according to conventional theory, and the relaxation oscillation frequency becomes purely imaginary [17]. Surprisingly, as we show in this Rapid Communication, it is under these conditions that the elusive RNGH instability can be observed. We show that quantum cascade lasers (QCLs) are uniquely suited for studying these coherent effects which, along with spatial hole burning (SHB), become a key factor in dictating the dynamics of the laser.

QCLs, because they are based on ultrafast tunneling and phonon-limited intersubband transitions, belong to the class of lasers which have an extremely fast gain recovery, in the range of a few ps [18]. Recent experiments showed indeed that the gain recovers within a few ps, which is approximately an order of magnitude shorter than the cavity round-trip time [19]. Since its invention in 1994, QCLs have undergone tremendous improvement [20]. Recent development of low loss, high power QCLs [21,22] enables the study of previously under investigated aspects, such as the richness of the optical spectrum and the ultrafast dynamics of these devices. In Ref. [23], strong evidence of self-pulsations at the cavity round-trip frequency was reported in QCLs, in par-

*Electronic address: kaertner@mit.edu

†Electronic address: capasso@deas.harvard.edu

 ©2007 The American Physical Society

ticular a large broadening of the spectrum above the threshold of this instability was observed. However, no detailed pulse characterization was provided. The technological potential of QCLs calls for a better understanding of the interplay of various instabilities in the parameter regime dictated by these lasers. Moreover, the Rabi frequency in QCLs at the power levels of a few hundred mW is of the order of a few THz, much larger than the spacing of Fabry-Perot modes. Therefore coherent effects should be easily observable in QCLs.

In this Rapid Communication we present a clear experimental demonstration of a coherent instability, driven by the same mechanism as the RNGH instability. It is identified in the most direct manner, by demonstrating in the optical spectrum of QCLs a splitting corresponding to twice the Rabi frequency.

The instability observed differs in some aspects from the original RNGH instability [2,3]. The threshold of instability can be as low as a few tens of percent above the laser threshold, as shown in Fig. 1(a). In addition, the pure RNGH instability typically gives rise to spectra with one central mode and two sidebands separated from it by the Rabi frequency, whereas in our experiments we observed two peaks only, similarly to Ref. [11]. However, the mechanism of the instability is the same in essence, namely the Rabi oscillations of the population inversion due to coherent effects. The differences from the RNGH instability as it occurs in ideal conditions [2,3] can be attributed to the presence of saturable absorption and SHB.

The QCLs studied were fabricated from two different wafers (wafer nos. 3251 and 3252) grown by metalorganic vapor phase epitaxy. The devices were processed into buried heterostructure lasers, in which an insulating Fe-doped InP layer is regrown after etching of the ridges [21,22]. The active region of all the samples tested is based on a four-quantum-well design, which relies on a double phonon resonance to achieve population inversion [24]. Note, however, that the multimode operation described in the present paper was also observed with lasers based on so-called three-quantum-well designs [18]. Figure 1(a) shows the optical spectra of a laser operated in continuous wave (cw) at room temperature. The active region of this laser is 3 μm wide and its emission wavelength is close to 8.47 μm (wafer no. 3251). The laser was cleaved into a 3-mm-long bar and soldered with indium onto a copper heat sink. The spectra were measured by a Fourier transform infrared spectrometer (FTIR) equipped with a deuterated triglycine sulphate (DTGS) detector.

As shown in Fig. 1(a), the laser spectrum is single mode close to threshold and broadens as the pumping current increases, splitting into two separated humps. The difference between the weighted centers of the two peaks increases linearly as a function of the square root of the collected output power from one facet, as shown in Fig. 1(b) (square dots with the dashed line as its best fit). The Rabi angular frequency Ω_{Rabi} can be easily calculated using the formula $\Omega_{\mathrm{Rabi}}=\mu E/\hbar=\mu\sqrt{2nI_{\mathrm{ave}}/(c\epsilon)}/\hbar$, where μ is the electron charge times the matrix element of the laser transition (=2.54 nm). I_{ave} is the average intracavity intensity in the gain region, which can be derived from the measured output

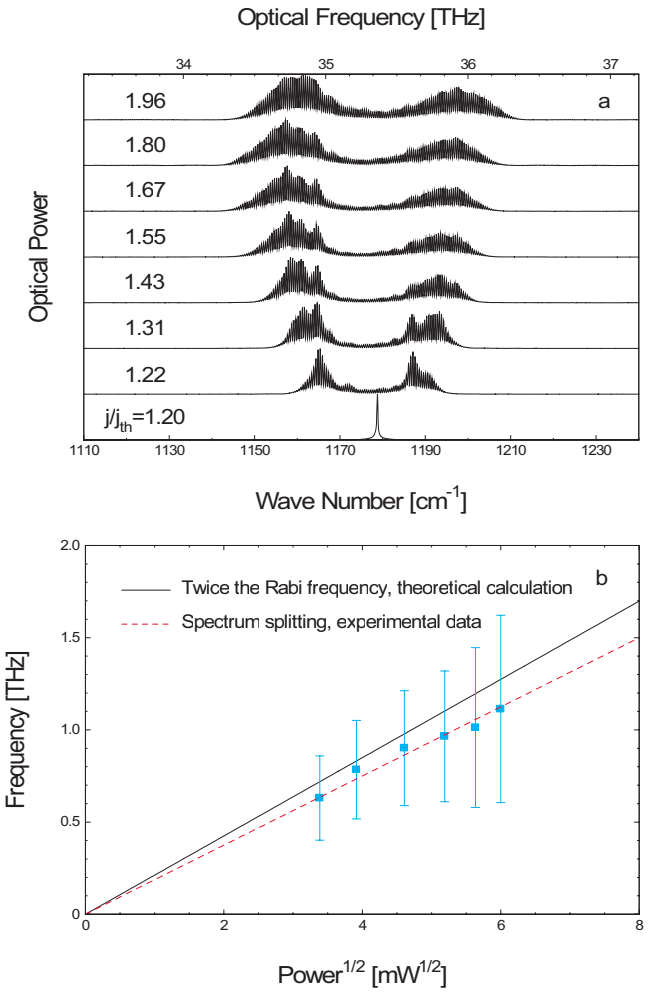

FIG. 1. (Color online) (a) Optical spectra vs pumping ratio (j/j_{th}) above threshold obtained in cw at 300 K with a 3-μm-wide buried heterostructure lasers emitting at 8.47 μm. For $1<j/j_{\mathrm{th}}<1.2$ the spectra are identical to $j/j_{\mathrm{th}}=1.2$. (b) Spectral splitting and twice the Rabi frequency $\Omega_{\mathrm{Rabi}}/(2\pi)$ vs square root of output power collected from a single laser facet. The different quantities reported on the graph were deduced from the experimental data shown in (a). The dashed line is a least-square linear fit of the data.

power. c is the speed of light in vacuum and n is the background refractive index. For all the values of the intensity corresponding to the spectra reported in Fig. 1(a), Ω_{Rabi} was calculated, multiplied by a factor 2 and then added to Fig. 2(b) (solid line). A very good agreement is found between the experimental splitting and twice the estimated Rabi frequency. Both curves fall indeed well within the error bars [25]. As mentioned before, the theory behind the RNGH instability predicts that the large intracavity intensity will result in parametric gain at frequencies detuned from the maximum of the gain curve by the Rabi frequency. The agreement mentioned above is thus a strong indication of the RNGH instability in QCLs.

In order to better understand the experimental spectra of the QCLs presented in Fig. 1(a), we use a simple model based on the standard one-dimensional Maxwell-Bloch equations [9], where the active medium is described by an "open" two-level system [26]. However, contrary to the standard

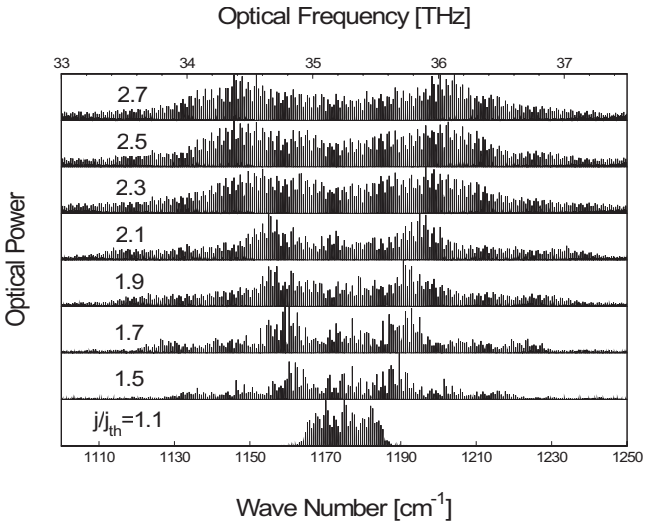

FIG. 2. Results of numerical simulations of the spectra based on the Maxwell-Bloch equations including a saturable absorber and spatial hole burning for different values of the current density normalized to the threshold value.

unidirectional Maxwell-Bloch equations, we allow the electromagnetic field to propagate in both directions. The waves traveling in the two directions are coupled, as they share the same gain medium. This gives rise to SHB [7]: The standing wave formed by a cavity mode imprints a grating in the gain medium through gain saturation. As a result, other modes become more favorable for lasing, and a multimode operation is triggered.

In the slowly varying envelope approximation, the equations read

$$\frac{n}{c}\partial_t E_\pm = \mp \partial_z E_\pm - i\frac{kN\mu\Gamma}{2\epsilon_0 n^2}\eta_\pm - \frac{1}{2}\ell(E_+,E_-)E_\pm, \tag{1a}$$

$$\partial_t \eta_\pm = \frac{i\mu}{2\hbar}(\Delta_0 E_\pm + \Delta_2^\pm E_\mp) - \frac{\eta_\pm}{T_2}, \tag{1b}$$

$$\partial_t \Delta_0 = \frac{\Delta_p - \Delta_0}{T_1} + \frac{i\mu}{\hbar}(E_+^*\eta_+ + E_-^*\eta_- - \text{c.c.}), \tag{1c}$$

$$\partial_t \Delta_2^\pm = \pm i\frac{\mu}{\hbar}(E_+^*\eta_- - \eta_+^* E_-) - \frac{\Delta_2^\pm}{T_1}. \tag{1d}$$

The + and − subscripts label the two directions of propagation. E and η are the slowly varying envelopes of the electric field and the polarization, respectively. The actual electric field and polarization are obtained by multiplying E and η by $e^{i\omega t}$ (ω is the optical resonance frequency) and taking the real part. The position-dependent inversion is written as the sum of the three terms, Δ_0, $\Delta_2^+ e^{2ikz}$, and $\Delta_2^- e^{-2ikz}$, where $(\Delta_2^+)^* \equiv \Delta_2^-$. The inversion is thereby represented by two slowly varying functions (Δ_0 and Δ_2^+), and $e^{\pm 2ikz}$ gives the fast variation in space. All the quantities mentioned so far are functions of space z and time t.

$\ell(E_+,E_-)$ is the loss in the cavity (not including the mirror loss), which is allowed to be nonlinear and dependent on the intensity. In this work we assume

$$\ell(E_+,E_-) = \ell_0 - \gamma(|E_+|^2 + |E_-|^2), \tag{2}$$

where ℓ_0 is the linear loss and γ is the self-amplitude modulation coefficient characterizing the nonlinear (saturable) part of the loss. Such a saturable absorption mechanism can come from Kerr lensing [8,23], caused by a nonlinear refractive index n_2 in the active region. As the intensity increases, the mode is more confined in the plane transverse to the propagation direction, and the net gain it experiences is greater. The reason is twofold: First, the mode overlaps more with the active region, leading to a larger modal gain (this mechanism is often called "soft Kerr lensing" [27]). Second, the overlap with the metal contacts is smaller, leading to smaller losses [23].

E_+ and E_- satisfy the boundary conditions $E_+ = rE_-$ at the $z=0$ boundary and $rE_+ = E_-$ at the $z=L$ boundary (L is the cavity length and $r \approx 0.53$ is the reflection coefficient). The other quantities in Eq. (1) are constants: k, N, and Γ are the wave number (in the material) associated with the resonance optical frequency, the electron density in the active region, and the overlap factor between the laser mode and the active region, respectively.

Figure 2 shows spectra that were obtained by solving numerically Eqs. (1) with the following parameters: for the saturable absorber, we used $\gamma = 10^{-8}\ \frac{\text{cm}}{\text{V}^2}$, obtained from two-dimensional mode simulations, assuming a $n_2 \approx 10^{-9}\ \frac{\text{cm}^2}{\text{W}}$ [23]. The index change due to this n_2 at typical intracavity intensities is about 10^{-3}. The other parameters are $\ell_0 = 5\ \text{cm}^{-1}$, $T_1 = 0.5$ ps [19], $T_2 = 0.07$ ps (corresponding to a gain full width at half maximum bandwidth of 4.8 THz), $L = 0.3$ cm, and $n = 3$, which are typical values for these lasers. N and Γ are not needed as long as the pumping is expressed relative to the lasing threshold. Note that the simulated spectra presented in Fig. 2 are averaged over about a microsecond. Only then does the average spectrum reach a steady state and a clear pattern shows up. The averaging is motivated by the fact that experimentally the spectra are acquired over an even much longer time scale. The envelopes of the spectra show two clear peaks whose separation compares well with twice the Rabi frequency, similarly to the experiment.

The lowering of the RNGH instability threshold by a saturable absorber can be established analytically by means of linear stability analysis. We propose this mechanism as the main reason for the observation of the RNGH instability at much lower pumping than RNGH theory predicts. In order to support this idea, we now present spectra from another device similar to the one described previously. The only difference between the two lasers is a shorter optical wavelength (5.25 μm) (wafer no. 3252) and a wider active region (5 μm). The two-dimensional waveguide simulations indicate a much weaker Kerr-lensing effect in these QCLs (γ is smaller by a factor of 4), due to the much larger ratio of active region width to wavelength. The measured optical spectra obtained at 300 K in cw mode with the 5-μm device

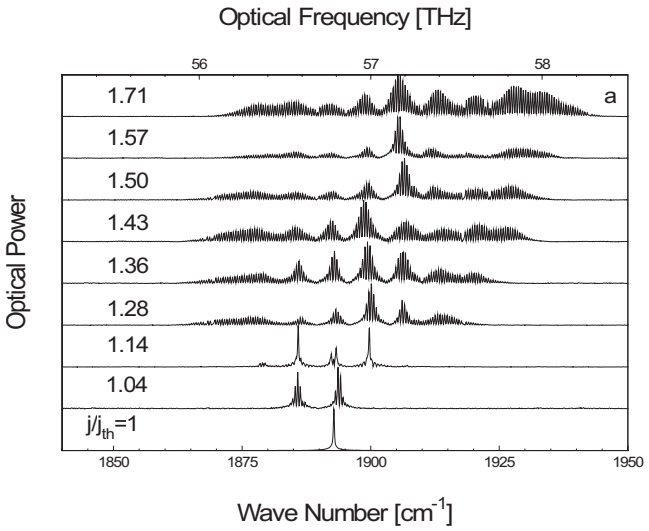

FIG. 3. Optical spectra vs pumping ratio above threshold obtained in cw at 300 K with a 5-μm-wide buried heterostructure lasers emitting at 5.25 μm.

are shown in Fig. 3. The data clearly show that the laser is at first single mode close to threshold and becomes multimode immediately after a slight increase of the pumping current. The envelopes of the spectra consist of multiple peaks, with an average separation 0.2 THz, independently of the pumping. Numerical integration of Eq. (1) without a saturable absorber ($\gamma=0$) leads to spectra that qualitatively agree with the ones in Fig. 3.

Reference [15] suggested that the suppression of the central peak in RNGH-type spectra can be due to the complex level structure of the gain medium, a dye molecule in that case. We show that SHB can also result in the suppression of the central peak (Fig. 2).

Our postulation of saturable absorption due to Kerr-lensing is supported by more extensive study of different devices beyond those shown in this Rapid Communication. First, we observed that for the same emission wavelength, a broad active region leads to a less pronounced RNGH-type signature. Second, we have also tested several standard ridge waveguide QCLs, for which the sidewalls of the ridges are covered by the gold contact. For these devices the coupling between the optical mode and the metal is expected to be stronger and so is the effect of saturable absorber due to Kerr lensing. The spectral behavior observed in this class of devices is dominated by RNGH-type instability.

In summary, a coherent multimode instability in quantum cascade lasers (QCLs) has been observed. It is similar in many ways to the Risken-Nummedal-Graham-Haken (RNGH) instability. The threshold of the observed phenomenon is significantly lower than in the original RNGH instability, which is attributed to the presence of a saturable absorber in the laser. For devices with a weaker saturable absorber, the envelope of the optical spectrum consists of many maxima whose separations are independent of the intracavity power. The nontrivial shape of the spectrum can be explained by SHB.

Support from the U.S. Army Research Laboratory and the U.S. Army Research Office under Grant No. W911NF-04-1-0253 is gratefully acknowledged. Part of the device processing was done at the Center for Nanoscale Systems (CNS) at Harvard University. Harvard-CNS is a member of the National Nanotechnology Infrastructure Network (NNIN).

[1] A. Z. Grasiuk and A. N. Oraevsky, *Proceedings of the VI International Congress on Microwave Tubes*, Scheveningen, Holland, 1962.
[2] H. Risken and K. Nummedal, J. Appl. Phys. **39**, 4662 (1968).
[3] P. Graham and H. Haken, Z. Phys. **213**, 420 (1968).
[4] H. Haken, *Synergetics* (Springer, New York, 1983).
[5] Ya. I. Khanin, *Principles of Laser Dynamics* (North-Holland, Amsterdam, 1996).
[6] H. Haken, Phys. Lett. **53A**, 77 (1975).
[7] A. Yariv, *Quantum Electronics*, 3rd ed. (John Wiley and Sons, New York, 1989).
[8] H. A. Haus, IEEE J. Sel. Top. Quantum Electron. **6**, 1173 (2000).
[9] L. Allen and J. H. Eberly, *Optical Resonance and Two Level Atoms* (Dover, New York, 1987).
[10] C. O. Weiss and J. Brock, Phys. Rev. Lett. **57**, 2804 (1986).
[11] L. W. Hillman, J. Krasiński, R. W. Boyd, and C. R. Stroud, Jr., Phys. Rev. Lett. **52**, 1605 (1984).
[12] E. H. M. Hogenboom, W. Klische, C. O. Weiss, and A. Godone, Phys. Rev. Lett. **55**, 2571 (1985).
[13] E. M. Pessina, G. Bonfrate, F. Fontana, and L. A. Lugiato, Phys. Rev. A **56**, 4086 (1997).
[14] T. Voigt, M. O. Lenz, F. Mitschke, E. Roldán, and G. J. de Valcŕcel, Appl. Phys. B: Lasers Opt. **79**, 175 (2004).
[15] H. Fu and H. Haken, J. Opt. Soc. Am. B **5**, 899 (1988).
[16] E. Roldán, G. J. de Valcárcel, J. F. Urchueguia, and J. M. Guerra, J. Opt. Soc. Am. B **20**, 816 (2003).
[17] R. Paiella *et al.*, Appl. Phys. Lett. **79**, 2526 (2001).
[18] F. Capasso, C. Gmachl, D. L. Sivco, and A. Y. Cho, Phys. Today **55**(5), 34 (2002).
[19] T. Norris (private communication).
[20] F. Capasso *et al.*, IEEE J. Quantum Electron. **38**, 511 (2002).
[21] L. Diehl *et al.*, Appl. Phys. Lett. **88**, 201115 (2006).
[22] L. Diehl *et al.*, Appl. Phys. Lett. **89**, 081101 (2006).
[23] R. Paiella *et al.*, Science **290**, 1739 (2000).
[24] M. Beck *et al.*, Science **295**, 301 (2002).
[25] The main contribution to the error bars is due to the uncertainty in determining the position of the center of mass of the two lobes present in the optical spectra.
[26] R. W. Boyd, *Nonlinear Optics*, 2nd ed. (Academic Press, London, 2003).
[27] F. Salin, J. Squier, and M. Piché, Opt. Lett. **16**, 1674 (1991).